Lateral Mixing in the Pycnocline by Baroclinic Mixed Layer Eddies

GUALTIERO BADIN

Department of Earth Sciences, Boston University, Boston, Massachusetts

AMIT TANDON

Department of Physics and Department of Estuarine and Ocean Sciences, University of Massachusetts—Dartmouth, North Dartmouth, Massachusetts

AMALA MAHADEVAN

Department of Earth Sciences, Boston University, Boston, Massachusetts

(Manuscript received 10 January 2011, in final form 16 May 2011)

ABSTRACT

Using a process study model, the effect of mixed layer submesoscale instabilities on the lateral mixing of passive tracers in the pycnocline is explored. Mixed layer eddies that are generated from the baroclinic instability of a front within the mixed layer are found to penetrate into the pycnocline leading to an eddying flow field that acts to mix properties laterally along isopycnal surfaces. The mixing of passive tracers released on such isopycnal surfaces is quantified by estimating the variance of the tracer distribution over time. The evolution of the tracer variance reveals that the flow undergoes three different turbulent regimes. The first regime, lasting about 3–4 days (about 5 inertial periods) exhibits near-diffusive behavior; dispersion of the tracer grows nearly linearly with time. In the second regime, which lasts for about 10 days (about 14 inertial periods), tracer dispersion exhibits exponential growth because of the integrated action of high strain rates created by the instabilities. In the third regime, tracer dispersion follows Richardson's power law. The Nakamura effective diffusivity is used to study the role of individual dynamical filaments in lateral mixing. The filaments, which carry a high concentration of tracer, are characterized by the coincidence of large horizontal strain rate with large vertical vorticity. Within filaments, tracer is sheared without being dispersed, and consequently the effective diffusivity is small in filaments. While the filament centers act as barriers to transport, eddy fluxes are enhanced at the filament edges where gradients are large.

1. Introduction

In the oceanic mixed layer (ML), atmospheric forcing, ocean dynamics, and their interplay act to leave the surface waters well mixed. While the ML waters are mixed in the vertical, lateral gradients in temperature and salinity are a common feature. Processes responsible for the creation of lateral gradients in temperature and salinity in the open ocean include nonhomogeneous heat and freshwater fluxes, wind mixing associated with the passage of a storm, and ocean convection. Near the coast, the upwelling of deep water, tidal mixing, and estuarine advection of freshwater create lateral gradients in properties. Such horizontal gradients in the temperature and salinity can compensate each other in their contribution to density (Rudnick and Ferrari 1999) or give rise to ML density fronts.

ML fronts in the ocean are dynamically unstable. They evolve in response to geostrophic adjustment (Tandon and Garrett 1994, 1995; Young 1994) while undergoing baroclinic instability (Molemaker et al. 2005; Boccaletti et al. 2007) and frontogenesis (Hoskins and Bretherton 1972; Capet et al. 2008a,b). A departure from quasi-geostrophic dynamics in the ML results in rich submesoscale dynamics. Frontogenesis, which can be enhanced through interaction with the mesoscale strain field (Bishop 1993; McWilliams et al. 2009a,b), is able to transfer energy from the mesoscale to the small scales where it is dissipated (Capet et al. 2008c). Fronts give rise to submesoscale

---

Corresponding author address: Gualtiero Badin, Department of Earth Sciences, Boston University, 675 Commonwealth Ave., Boston, MA 02215.
E-mail: gualti@bu.edu

DOI: 10.1175/JPO-D-11-05.1

filaments of intense vertical vorticity with enhanced vertical velocities (Spall 1997; Mahadevan and Tandon 2006), which are significant for the transfer of nutrients to the surface euphotic layer (Levy et al. 2001). The ageostrophic secondary circulation that results in vertical velocities can be further intensified by vertical mixing (Nagai et al. 2006) and nonlinear Ekman effects (Thomas and Lee 2005). The presence of weak stratification and large vertical shears in the ML leads to ageostrophic baroclinic instabilities (Stone 1966, 1970, 1971), which have much faster growth rates than baroclinic instability in the pycnocline (Boccaletti et al. 2007). Despite being adiabatic, ML baroclinic instability results in the restratification of the ML (Fox-Kemper et al. 2008).

In contrast to earlier studies that have focused on the role of submesoscale dynamics on vertical advection and mixing, as well as the rearrangement of buoyancy in the ML, the aim of this study is to infer the importance of submesoscale dynamics on lateral mixing along isopycnal surfaces in the oceanic pycnocline. This is motivated by observations in which rates of lateral mixing were found to be time and scale dependent (Okubo 1970), and the inferred horizontal diffusivity far exceeded the values that could be explained by shear dispersion (Sundermeyer and Price 1998). What are the processes that lead to enhanced lateral dispersion on scales of 0.1–10 km? Is such mixing driven by dynamical instabilities and thereby associated with the growth and evolution of such instabilities? It has been previously hypothesized that enhanced lateral mixing in the pycnocline results from the generation of mixed patches generated by internal wave breaking that spin up under the action of gravity and rotation to form vortical modes or eddies (Sundermeyer et al. 2005; Sundermeyer and Lelong 2005). In this study, we neglect vortical modes, and instead examine lateral mixing resulting from the submesoscale flow field generated by ML eddies.

A natural question is to ask whether the submesoscale dynamics of the ML can impact the pycnocline. We address this question with a modeling process study of the ML and pycnocline within a limited domain (approximately 200 km × 100 km). Our three-dimensional numerical ocean model is initialized with a zonally oriented ML front, overlying an initially quiescent pycnocline with flat isopycnals. The model domain is a zonally periodic channel. The ML is chosen to be deep ($\sim$200 m) so as to generate a submesoscale flow field without any forcing. The model setup is described in section 3 and in the appendix. The numerical experiments capture the growth of submesoscale instabilities resulting in the spindown of the front. In contrast, oceanic flows are highly developed and most often forced by surface fluxes. Yet, submesoscale instabilities are frequently triggered on the edges of mesoscale fronts and meanders as evidenced in high-resolution satellite imagery. We think of this process study as examining lateral mixing during the growth phase of submesoscale ML instability, which could be viewed as growing on the edge of an underlying mesoscale feature.

In what follows, we present the analysis of numerical experiments used to infer tracer mixing that is driven by submesoscale ML eddies generated from various frontal configurations. In section 2 we also review theoretical results for tracer dispersion and particle statistics that are useful for understanding tracer dispersion the submesoscale context. A reader familiar with these could skip directly to section 3, which describes our numerical experiments. Our results, in section 4a, start with a description of submesoscale signatures in the pycnocline arising from surface ML instabilities. To study mixing, we introduce a passive tracer along the initially flat isopycnal surfaces at various depths below the ML. As the flow develops, we use the evolution of the dye distribution to infer the rate of lateral mixing. Our methods of analysis are based on previous observational studies where dye was used to infer lateral mixing—for example, during the North Atlantic Tracer Release Experiment (NATRE) (Ledwell et al. 1998; Sundermeyer and Price 1998; Polzin and Ferrari 2004) and on the New England continental shelf (Houghton 1997; Sundermeyer and Ledwell 2001; Ledwell et al. 2004). Since the ML front and geostrophic flow field are oriented west to east, and since our model domain is zonally periodic, we lay down the dye in east–west, x-oriented streaks across the domain, and estimate dispersion in the cross-front, y direction. We then describe the time evolution of the tracer concentration variance for streaks of tracer released on different isopycnal surfaces in section 4b. We use the variance analysis to obtain an integrated measure of lateral mixing and assess its dependence on ML dynamics. The mixing invoked by this mechanism is compared with values estimated for other processes in section 4c. In section 4d, we estimate the effective diffusivity of an individual filament to mechanistically understand the structure and role of submesoscale filaments in mixing. Finally, we present some points of discussion and our conclusions in sections 5 and 6.

2. Theoretical background

a. ML instabilities

In the oceanic ML, ageostrophic baroclinic instability gives rise to dynamical features such as ML eddies and submesoscale filaments with typical length scales ($L_s \sim$ 1–10 km) that are much smaller than the Rossby radius of deformation ($L_d \sim$ 10–100 km) associated with the pycnocline. Submesoscale dynamics are characterized by the Rossby (R_0) and Richardson (Ri) numbers attaining $O(1)$ values locally, where $R_0 \equiv \zeta/f$ is the ratio of the vertical component of relative vorticity $\zeta = v_x - u_y$ to planetary vorticity f, and $\mathrm{Ri} \equiv N^2/U_z^2$, where $U_z^2 = u_z^2 + v_z^2$ is the square of the vertical shear of the horizontal velocity (u, v). The vertical and horizontal gradients of the buoyancy $b \equiv -g[(\rho - \rho_0)/\rho_0]$, defined in terms of the density ρ and a reference value ρ_0, give the square of the buoyancy frequency, $N^2 = b_z$ and its horizontal equivalent, defined here only in terms of the cross-front direction as $M^2 = b_y$. For an ML front aligned in the zonal direction and in thermal wind balance, $\mathrm{Ri} \sim O(1)$ gives rise to the balance (Tandon and Garrett 1994; Young 1994; Tandon and Garrett 1995)

$$N^2 \sim \frac{M^4}{f^2}. \tag{1}$$

Such fronts develop large relative vorticity $[\zeta \sim O(f)]$ and exhibit ageostrophic baroclinic instability, as studied by Stone (1966, 1970, 1971). The growth rate of the ageostrophic instabilities (Eldevik and Dysthe 2002) in terms of Ri and the Burger number $\mathrm{Bu} = (L_s/L)^2$, where L is the width of the front and $L_s = M^2H/f^2$ is the Rossby radius within the ML of depth H, is given by

$$\sigma_t = f\left(\frac{5/54}{1 + \mathrm{Ri} + \mathrm{Ri}\cdot\mathrm{Bu}}\right)^{1/2}. \tag{2}$$

The wavelength for the linear growth of the most unstable perturbation is given by (Eldevik and Dysthe 2002)

$$\lambda = \phi_0 L_s\left(1 + \frac{1}{\mathrm{Ri}} + \frac{\mathrm{Bu}}{2}\right)^{1/2}, \tag{3}$$

where $\phi_0 = 4\pi/\sqrt{10} \approx 4$.

For Bu = 0, (2) reduces to the formula for the growth rate found by Stone (1966), which compares well with the analytical solutions found by Eady (1949) and Fjørtoft (1950) for $\mathrm{Ri} \gg 1$ and Ri = 0, respectively. It should be noted that ML instabilities act to modify both b_y and the ML depth H through restratification (Boccaletti et al. 2007; Fox-Kemper et al. 2008; Mahadevan et al. 2010), altering both Ri and Bu, and thereby the growth rate of the ML instabilities according to (2).

Given (1) and the thermal wind balance $u_z = -b_y/f$, where u is the alongfront velocity, the cross-front eddy velocity v' scales as (Haine and Marshall 1998; Fox-Kemper et al. 2008)

$$v' \sim |u| \sim |u_z|H \sim \frac{M^2H}{f}, \tag{4}$$

where H is the initial depth of the ML. It can thus be seen that the submeso length scale associated with the inertial time scale $\sim O(f^{-1})$ is given by $L_S \sim M^2H/f^2$. While these scaling arguments apply to the ML, the theory can be extended to estimate the vertical extent of the signatures into the pycnocline. Scaling (Pedlosky 1987) suggests that the e-folding depth of penetration for an ML eddy is

$$D \approx \frac{fL_s}{N}, \tag{5}$$

where N, the buoyancy frequency in the pycnocline, is assumed to be uniform.

b. Turbulent dispersion of tracers

To examine the effect of submesoscale ML eddies on lateral mixing, we consider the evolution of a tracer with concentration $C(x, y, z, t)$ as described by the advection–diffusion equation

$$\frac{\partial C}{\partial t} + \mathbf{u}\cdot\nabla C = \nabla_H\cdot(\kappa_H\nabla_H C) + \frac{\partial}{\partial z}\left(\kappa_z\frac{\partial C}{\partial z}\right), \tag{6}$$

where κ_H is the horizontal diffusivity of the tracer, assumed to be isotropic, and κ_z is the vertical diffusivity of the tracer. Because the slope of isopycnal surfaces in the pycnocline is extremely small, it will suffice to consider the analysis in 2D (x, y), while projecting C and the horizontal velocity (u, v) onto the isopycnal surfaces. We focus on along-isopycnal (2D) dispersion of tracer because the ML instabilities are adiabatic, particularly in the pycnocline. Calculations in which we included the vertical displacement of tracer showed no departure from our 2D results.

Moments of the tracer concentration are used to study the turbulent dispersion of the tracer along an isopycnal surface in response to the eddying flow (Thiffeault 2008). Using the notation $\langle\cdot\rangle = \int(\cdot)\,dx\,dy|_\rho$, the zero moment $\langle C\rangle$ defines the total amount of tracer, such that $\partial_t\langle C\rangle = 0$ for a conserved tracer.

The zonal periodicity of our numerical experiments lends itself to a simplification; we need consider only the meridional (y directional) moments. The vector of first moments and tensor of second moments are, thus, both reduced to just one component each. The first moment, normalized by the total tracer

$$\sigma_y = \frac{\langle yC\rangle}{\langle C\rangle}, \tag{7}$$

defines the y displacement of the center of mass of the tracer. The second moment (normalized by the total tracer) minus the first moment squared,

$$\sigma_{yy} = \frac{\langle y^2 C\rangle}{\langle C\rangle} - \sigma_y^2, \qquad (8)$$

defines the tracer variance or dispersion in the y direction. Fickian diffusivity would cause tracer dispersion (σ_{yy}) to increase linearly with time as $(\partial/\partial t)\sigma_{yy} \sim K_y$, where K_y is the diffusivity.

c. Particle statistics

Particle statistics offers a theoretical basis for understanding dispersion. Passive tracer dispersion statistics can be analyzed in terms of the statistical history of neutrally buoyant particles without inertia. For example, the method was used to study tracer dispersion by surface waves (Herterich and Hasselmann 1982). If particles are seeded in a patch of passive tracer, after an initial diffusion time the particles and the tracers will have the same domain of occupation (Garrett 1983). The dispersion of a patch of particles is a function of the strain rate $\gamma = [(u_x - v_y)^2 + (v_x - u_y)^2]^{1/2}$. Initially, for time $t < O(\gamma^{-1})$ the patch grows diffusively (Garrett 1983). The initial period of small-scale diffusion lasts until the time that the tracer patch begins to be influenced by submesoscale strain. For submesoscale dynamics, $\gamma = O(f)$ (Mahadevan and Tandon 2006), so that for $f = 10^{-4}$ s^{-1} the initial diffusion period for the tracer caught in a submesoscale filament is only about 0.1 days. However, the tracer streak is caught by an ensemble of several intermittent filaments, resulting in a weaker ensemble strain, which results in a longer diffusive period.

The theory of dispersion statistics described in Bennett (1984) and LaCasce (2008) allows us to study the evolution and transition of dispersive behavior in time. Taking two particles with initial separation in the meridional direction y_0 at the initial time t_0, the relative diffusivity of the particles K_y at a later time $t > t_0$ is defined as (Taylor 1921)

$$K_y \equiv \frac{1}{2}\frac{d}{dt}\langle y^2\rangle = \langle y_0 v\rangle + \int_{t_0}^{t} \langle v(t)v(\tau)\rangle\, d\tau, \qquad (9)$$

where $y^2(t)$ is the relative dispersion of the particles, $v = (d/dt)y$ is the pair separation velocity, and the link between particle statistics and passive tracer is given by $y^2(t) \sim \sigma_{yy}(t)$. Following Bennett (1984), it is possible to express the mean square separation velocity as

$$\left\langle \left(\frac{d}{dt}y\right)^2 \right\rangle = 2\int_0^\infty E(k)[1 - J_0(ky)]\, dk, \qquad (10)$$

where $E(k)$ is the Eulerian kinetic energy wavenumber spectrum and J_0 is the first Bessel function. When the particle separation scale is smaller than the length scale of eddies then $ky \ll 1$ and $1 - J_0 \approx (1/4)k^2y^2$. When the separation scales larger than the eddy length scale then $ky \gg 1$ and $1 - J_0 \approx 1$. Assuming the power law dependence $E(k) \propto k^{-\alpha}$, (10) can be separated as

$$\left\langle \left(\frac{d}{dt}y\right)^2 \right\rangle = 2\int_0^{1/y} k^{-\alpha}\left(\frac{1}{4}k^2y^2\right)dk + 2\int_{1/y}^{\infty} k^{-\alpha}dk, \qquad (11)$$

which has solution

$$\left\langle \left(\frac{d}{dt}y\right)^2 \right\rangle = \frac{1}{2}y^2\frac{1}{3-\alpha}k^{3-\alpha}\Big|_0^{1/y} + \frac{2}{1-\alpha}k^{1-\alpha}\Big|_{1/y}^{\infty}. \qquad (12)$$

The first term of (12) diverges for $\alpha \geq 3$, while the second term diverges for $\alpha \leq 1$. As noted by Bennett (1984) and LaCasce (2008), for intermediate values of the spectral slope $1 < \alpha < 3$,

$$\left\langle \left(\frac{d}{dt}y\right)^2 \right\rangle \propto y^{\alpha-1}, \qquad (13)$$

so that

$$K_y \propto y^{(\alpha+1)/2}. \qquad (14)$$

The dependence of K_y on the particle separation thus directly reflects the spectral slope α. In this case the dispersion of particle pairs is dominated by eddies of the same size as the separation and the dispersion is termed "local." For $\alpha \geq 3$ the dispersion is dominated by eddies larger than the separation scale and it is called "non local." Given a certain spectral slope α, Eq. (12) and, consequently, (9) can be solved at different stages of evolution of the flow as follows.

1) EARLY TIME

At early times, the particles are very close and the velocity difference between the particles is approximately constant. The tracer experiences Brownian-like dispersion. Following Einstein (1905) and Taylor (1921), for K_y constant, σ_{yy} varies linearly in time as

$$\sigma_{yy} = 4K_y t. \qquad (15)$$

2) INTERMEDIATE TIME

At intermediate times, the nearest particle pair velocities are mutually correlated, but the particle separation scale is still much smaller than the length scale of eddies. In this period, the KE spectra has k^{-3} dependence (Kraichnan and Montgomery 1980) and $ky \gg 1$, so that (12) and (9) give (Lin 1972)

$$\sigma_{yy} = \exp(C_1\eta^{1/3}t) \quad \text{and} \tag{16}$$

$$K_y = C_1\eta^{1/3}\sigma_{yy}, \tag{17}$$

where C_1 is a nondimensional constant, $\eta = \nu_h\langle|\nabla\zeta|^2\rangle$ is the enstrophy dissipation rate, and ν_h is the momentum viscosity. This period is also referred to as the enstrophy inertial range. The exponential growth of relative dispersion (16) would also be expected for 3D turbulence, but at much smaller scales than the scales resolved in our numerical experiment.

3) LATER TIME

When the particle separation reaches synoptic scales, for 2D turbulence and $ky \ll 1$ the KE spectra has $k^{-(5/3)}$ dependence, so that (12) and (9) give (Richardson 1926; Batchelor 1950)

$$\sigma_{yy} = C_2\epsilon t^3 \quad \text{and} \tag{18}$$

$$K_y = C_2^{1/3}\epsilon^{1/3}\sigma_{yy}^{2/3}, \tag{19}$$

where C_2 is a nondimensional constant and $\epsilon = \nu_h\langle(\nabla\mathbf{u})^2\rangle$ is the energy dissipation rate. Equation (18) is referred to as Richardson's power law, while (19) represents Richardson's $4/3$ law for the particle separation y since $\sigma_{yy} \sim y^2$. This regime is also referred to as the energy inertial range.

The presence of different turbulent regimes is controversial, both in the context of the atmosphere and the ocean. In the atmosphere, the exponential growth described by (16) has been observed by balloon experiments launched near the tropopause in the Southern Hemisphere (Morel and Larcheveque 1974; Er-El and Peskin 1981). Lacorata et al. (2004), however, making use of finite-scale Lyapunov exponents, reanalyzed the same dataset to find that the growth followed Richardson's law (18). In the ocean, exponential growth has been observed in the Gulf Stream region by subsurface floats (LaCasce and Bower 2000). However, Ollitrault et al. (2005) and Lumpkin and Elipot (2010) found Richardson growth in the same region. Richardson's law has been observed, for example, by Stommel (1949), while exponential growth has also been observed by J. Price (1981, unpublished manuscript) though dye release experiments in the ML. Further, a transition from exponential to Richardson-type growth has been observed by surface drifters in the Nordic Seas by Koszalka et al. (2009).

Finally, in the quasi-geostrophic limit, turbulence theory predicts that both active tracers (e.g., enstrophy) and passive tracers are cascaded with horizontal to vertical aspect ratio N/f (Kraichnan 1967; Haynes and Anglade 1997; Smith and Ferrari 2009).

d. *Effective diffusivity of tracers*

Effective diffusivity (Nakamura 1996; Winters and D'Asaro 1996) is related to the complexity of the shape of the area occupied by a certain value of tracer concentration. Even though the effective diffusivity is calculated as a function of tracer concentration, it is useful in characterizing the role of specific spatial structures on mixing. Effective diffusivity has been employed to study the mixing of tracers by idealized Kelvin–Helmoltz billows (Nakamura 1996; Winters and D'Asaro 1996)—the stratospheric and tropospheric transport and mixing of tracers in different dynamical regimes. Chaotic advection and the role of stratospheric polar vortices as barriers to mixing tracers have been studied through both observations (Nakamura and Ma 1997; Haynes and Shuckburgh 2000a,b) and modeled flows (Shuckburgh and Haynes 2003). It has also been used for oceanic jets along the Antarctic Circumpolar Current that are shown to act as barriers to mixing (Marshall et al. 2006; Shuckburgh et al. 2009).

Under the approximation that the evolution of a certain tracer concentration class C takes place along isopycnals in the interior, (6) can be written as a diffusion equation

$$\frac{\partial C}{\partial t} = \frac{\partial}{\partial A}\left(L_0^2 K_{\text{eff}}\frac{\partial C}{\partial A}\right) \tag{20}$$

in area coordinates, where $A(C, t)$ is the area of the tracer concentration class C and

$$K_{\text{eff}} = \kappa_H\frac{L_{\text{eq}}^2}{L_0^2} \tag{21}$$

is the effective diffusivity. In (20)–(21) we make the approximation that, along isopycnals in the interior, the along-isopycnal diffusivity is the same as the horizontal diffusivity κ_H. In (21), L_0^2 is the area corresponding to the minimum length of the tracer concentration class C contours, and

$$L_{\text{eq}}^2 = \frac{1}{\left(\dfrac{\partial C}{\partial A}\right)^2}\frac{\partial}{\partial A}\int_{A(C,t)}(\nabla C)^2\,dA \tag{22}$$

is the area corresponding to the contours of the tracer concentration C, deformed by the action of the straining velocity field. For a careful derivation of (21) and (22) see Nakamura (1996) and Winters and D'Asaro (1996).

Various approximations can be adopted to obtain a value for L_0^2. For the stratosphere, L_0^2 can be obtained because of the zonal symmetry of the flows and can be related to the slowest decaying mode of the diffusion equation on a sphere (Shuckburgh and Haynes 2003). For the Southern Ocean, the zonal distribution of tracer allows a definition of L_0^2 by applying a large horizontal diffusivity to the domain in order to maintain zonal symmetry (Marshall et al. 2006). In the present study, L_0^2 is calculated as the initial value of L_{eq}^2. However, it can be noted that K_{eff} is an integral measure: in a fully turbulent flow, regions belonging to the same tracer concentration class can be detached from each other (i.e., the flow changes its topology), and the deformation of a particular patch belonging to a certain tracer concentration class would result in assigning the same value of K_{eff} to other patches that are not experiencing deformation. To assign $K_{\mathrm{eff}} = 0$ to regions not experiencing deformation, K_{eff} should be analyzed by dividing the domains in smaller subdomains or—when the division into subdomains is not possible because, for example, of the dominance of advection—by paying extra care not to assign values of K_{eff} to regions that are not deformed by the flow. Furthermore, the domain-integrated value of K_{eff} increases initially and then reaches a maximum. The calculations presented in this study refer to the period when K_{eff} has reached a maximum and the tracer field has not already divided into patches.

3. Numerical experiments

We perform a number of numerical simulations of a deep, geostrophically balanced ML front that overlies a pycnocline, which is initially at rest with flat isopycnals. The model domain (of extent $L_x = 96$ km, $L_y = 192$ km, and depth = 500 m) is a periodic zonal channel with solid boundaries in the meridional (y) direction and a stratified interior overlying a flat bottom. The model grid uses 1-km horizontal resolution and 32 grid cells in the vertical that increase in size over depth. The domain is initialized with lighter water in the southern half of the ML and denser water to the north, with a vertical front separating the two regions. The initial velocity field is a geostrophically balanced frontal jet $[u(y, z)]$ within the ML with vertical shear ($u_z = -b_y/f$) in thermal wind balance; the interior is initially quiescent with flat isopycnals. The ML front evolves without any active wind or buoyancy forcing, (e.g., representing the spindown of an ML front created by the passage of a storm), which leads to genesis of ML eddies that restratify the ML. A three-dimensional, Boussinesq, free-surface, nonhydrostatic numerical model (Mahadevan et al. 1996a,b) is used with the same configuration as in Mahadevan et al. (2010). The model has constant horizontal momentum viscosity $\nu_h = 5\ \mathrm{m^2\ s^{-1}}$ and vertical viscosity $\nu_z = 10^{-5}\ \mathrm{m^2\ s^{-1}}$. The pycnocline is flat, with nonuniform stratification that has an initial maximum value of $N^2 = 1.8 \times 10^{-4}\ \mathrm{s^{-2}}$ at 240 m and decreasing to $N^2 = 10^{-5}\ \mathrm{s^{-2}}$ at 500 m. Full details of the model are reported in the appendix and in Table 1. A reference model integration using an initial lateral buoyancy gradient $b_{y0} = -0.9 \times 10^{-7}\ \mathrm{s^{-2}}$ and ML depth $H = 200$ m is the basis for the discussion in the next section, unless otherwise stated. Several numerical experiments with variations to these parameters were also performed, as summarized in Table 2. In the numerical integrations, the initial value of b_y ranges between $0.2b_{y0}$ and $5b_{y0}$, and H ranges between 100 and 200 m. Correspondingly, Ri and Bu range between Ri = 4×10^{-2} and Bu = 10^{-3} for the integration with $0.2b_{y0}$, and Ri = 25 and Bu = 4×10^{-3} for the integration with $5b_{y0}$.

TABLE 1. Model parameters.

f	Coriolis parameter	$10^{-4}\ \mathrm{s^{-1}}$
L_x	Horizontal scale of the channel	96×10^3 m
L_y	Meridional scale of the channel	192×10^3 m
H_{tot}	Total depth	500 m
H	Initial ML depth (reference integration)	200 m
ν_h	Horizontal eddy viscosity	$5\ \mathrm{m^2\ s^{-1}}$
ν_z	Vertical eddy viscosity	$10^{-5}\ \mathrm{m^2\ s^{-1}}$
κ_H	Horizontal diffusivity	$5\ \mathrm{m^2\ s^{-1}}$
κ_z	Vertical diffusivity	$5\ \mathrm{m^2\ s^{-1}}$
$\Delta\rho_0$	Initial density variation across front (reference integration)	$0.2\ \mathrm{kg\ m^{-3}}$
b_{y0}	Maximal lateral buoyancy gradient at front (reference integration)	$-0.9 \times 10^{-7}\ \mathrm{s^{-2}}$

a. Initialization of tracer for studies of dispersion

To study the lateral dispersion of tracer in the pycnocline, east–west-oriented streaks of tracer are laid down beneath the ML front along isopycnal surfaces $\sigma = 25.44$, 26.19, 26.54, and 26.76, which are at initial depths ranging from 217 to 355 m (see appendix for details). The streaks are initially 1 km wide (corresponding to 1 grid cell) and 96 km in length in order to extend across the entire domain, and of a concentration of 1 tracer unit. Details of the initialization of the tracer streaks are reported in the appendix and in Table 2. The dispersion of the tracer (σ_{yy}) is estimated along each of the isopycnal surfaces as a function of time and provides an integrated measure of tracer mixing by the submesoscale dynamics.

To test the sensitivity of the results to the initial tracer distribution, we performed experiments where the tracer streak width was given an initial Gaussian distribution over 10 km (10 grid cells) and a maximum concentration of 1 unit. Also, the sensitivity of our results to the numerical parameters in the model was tested by reducing both horizontal momentum viscosity and horizontal tracer diffusivity to $\nu_h = 1\ \mathrm{m^2\ s^{-1}}$ and $\kappa_H = 1\ \mathrm{m^2\ s^{-1}}$.

TABLE 2. Combinations of the initial cross-front buoyancy gradient b_y, ML depth H, horizontal viscosity ν_h, horizontal diffusivity κ_H, and initial tracer streak width W_0 used in numerical experiments. The reference integration is with $H = 200$ m, $b_{y0} = -0.9 \times 10^{-7}$ s^{-2}, $\nu_h = 5$ m^2 s^{-1}, $\kappa_H = 5$ m^2 s^{-1}, and $W_0 = 1$ km (1 grid cell) in meridional extent. Tracer was introduced on four isopycnal surfaces $\sigma = 25.44, 26.19, 26.54$, and 26.76 in the pycnocline. For the reference integration, the four isopycnal surfaces have an initial depth of 216.59, 256.88, 302.72, and 354.87 m, respectively. The 10-km-wide tracer streak has a Gaussian profile in meridional section with maximum value 1, whereas the 1-km-wide streak is simply initialized with concentration 1 within the grid cell.

H	b_y					ν_h	κ_H	W_0
200 m	$0.2b_{y0}$	$0.5b_{y0}$	$0.75b_{y0}$	b_{y0}	$5b_{y0}$	5 m^2 s^{-1}	5 m^2 s^{-1}	1 km
150 m	—	—	—	b_{y0}	—	5 m^2 s^{-1}	5 m^2 s^{-1}	1 km
100 m	—	—	—	b_{y0}	—	5 m^2 s^{-1}	5 m^2 s^{-1}	1 km
200 m	—	—	—	b_{y0}	—	1 m^2 s^{-1}	1 m^2 s^{-1}	1 km
200 m	—	—	—	—	$5b_{y0}$	1 m^2 s^{-1}	1 m^2 s^{-1}	1 km
200 m	—	—	—	b_{y0}	—	5 m^2 s^{-1}	5 m^2 s^{-1}	10 km
200 m	—	—	—	b_{y0}	—	1 m^2 s^{-1}	1 m^2 s^{-1}	10 km

b. Tracer initialization for estimation of effective diffusivity

To estimate an effective diffusivity (K_{eff}) we initialize a second tracer on the same isopycnals where the tracer streaks were laid down with a continuous distribution $C(y) = 1 - y/L_y$, where L_y is the meridional dimension of the domain and $0 \le y \le L_y$. Because K_{eff} depends on tracer concentration classes, this tracer, which varies linearly in the zonal direction from 1 to 0, allows us to visualize K_{eff} in the entire domain. During the numerical integration, the maximum concentration of tracer decreases exponentially, thus requiring a large number of classes of tracer concentration in order to resolve K_{eff} even when the maximum concentration of tracer reaches very small values. We use 50 classes of tracer concentration, each having a range of 1/50. A similar analysis with a larger number of tracer classes showed convergence, suggesting that 50 tracer classes are adequate.

4. Results

a. Growth of submesoscale instabilities

The ML front, which is initially oriented east–west, becomes unstable, forming meanders that are initially of a small wavelength, but grow as the instability develops and form eddies that act to restratify the ML, moving lighter water over denser water with minimal vertical mixing. Figures 1a–c show the evolution of the surface density field in the numerical model.

The initial linear growth rate of the ageostrophic instabilities in the model can be calculated in the linear growth regime as $\sigma_t = \log[\text{EKE}(t)]/2t$, where EKE is the eddy kinetic energy integrated over the ML. The resulting growth period for ML instabilities is $\sigma_t^{-1} \approx 0.4$ days. In comparison, (2) suggests a growth period for the ML instabilities of $\sigma_t^{-1} \approx 0.5$ days, estimated with $N^2 = 10^{-6}$ s^{-2}, Ri = 1, and Bu = 0.0023, where Bu is calculated using $L = 32$ km. Similarly, (3) gives a wavelength for the linear growth of the most unstable perturbation for the ML eddies of $\lambda = 1.1 \times 10^4$ m.

The ML eddies that develop from the instability of the front are seen to have a strong submesoscale character. The vertical component of the relative vorticity ζ and the lateral strain rate γ (Figs. 1d–i) are elevated in filaments where they attain values of $O(f)$. Notably, the elevated values of ζ and γ occur at the same location in filaments, undermining the physical basis for a separation of submesoscale flow into strain- and vorticity-dominated regions by the Okubo–Weiss parameter (Okubo 1970; Weiss 1991).

Vertical sections across the front, shown at various times of the simulation in Fig. 2, reveal that ML eddies slump the isopycnals (shown in black) at the front, causing restratification within the ML as they release the available potential energy associated with the lateral buoyancy gradient at the front. The vertical component of the relative vorticity ζ (shown in color) reveals that ML eddies are often, but not always, surface intensified; yet, they are able to penetrate into the pycnocline to result in the significant perturbation of isopycnal surfaces and an energetic adiabatic flow field that leads to vigorous lateral mixing of tracers. The evolution of the tracer streaks on two of the isopycnal surfaces as a result of such mixing is shown in cross section in Figs. 2d–f.

Figure 3 shows the effect of the ML eddies on relatively shallow and deep isopycnal surfaces, $\sigma = 25.44$ (Figs. 3a–c) and 26.76 (Figs. 3d–f), 20 days after the spindown of the front begins. Along $\sigma = 25.44$, the ML eddies induce large deformations (±30 m) in the initially flat isopycnal surface. Filaments with $|\zeta| \approx 0.5f$ and $\gamma \approx f$ are visible at the same location in regions with strong gradients in the anomalous isopycnal depth. Along $\sigma = 26.76$, the ML eddies deform the isopycnal (±10 m) and create filaments with $|\zeta| \approx 0.5f$ and $\gamma \approx 0.5f$. The positions of the dynamic filaments demarcated by elevated ζ and γ are not in the same location on the two isopycnals, but are vertically deflected by the stratification. The vertical deflection of the filaments by stratification and the development of thin horizontal layers of independent vortex dipoles (Fig. 3c) is possibly analogous to experimentally observed zigzag instabilities (Billant and Chomaz 2000a,b), which can grow in the presence of both a low horizontal Froude number and a high Reynolds number, which are present in our model simulation.

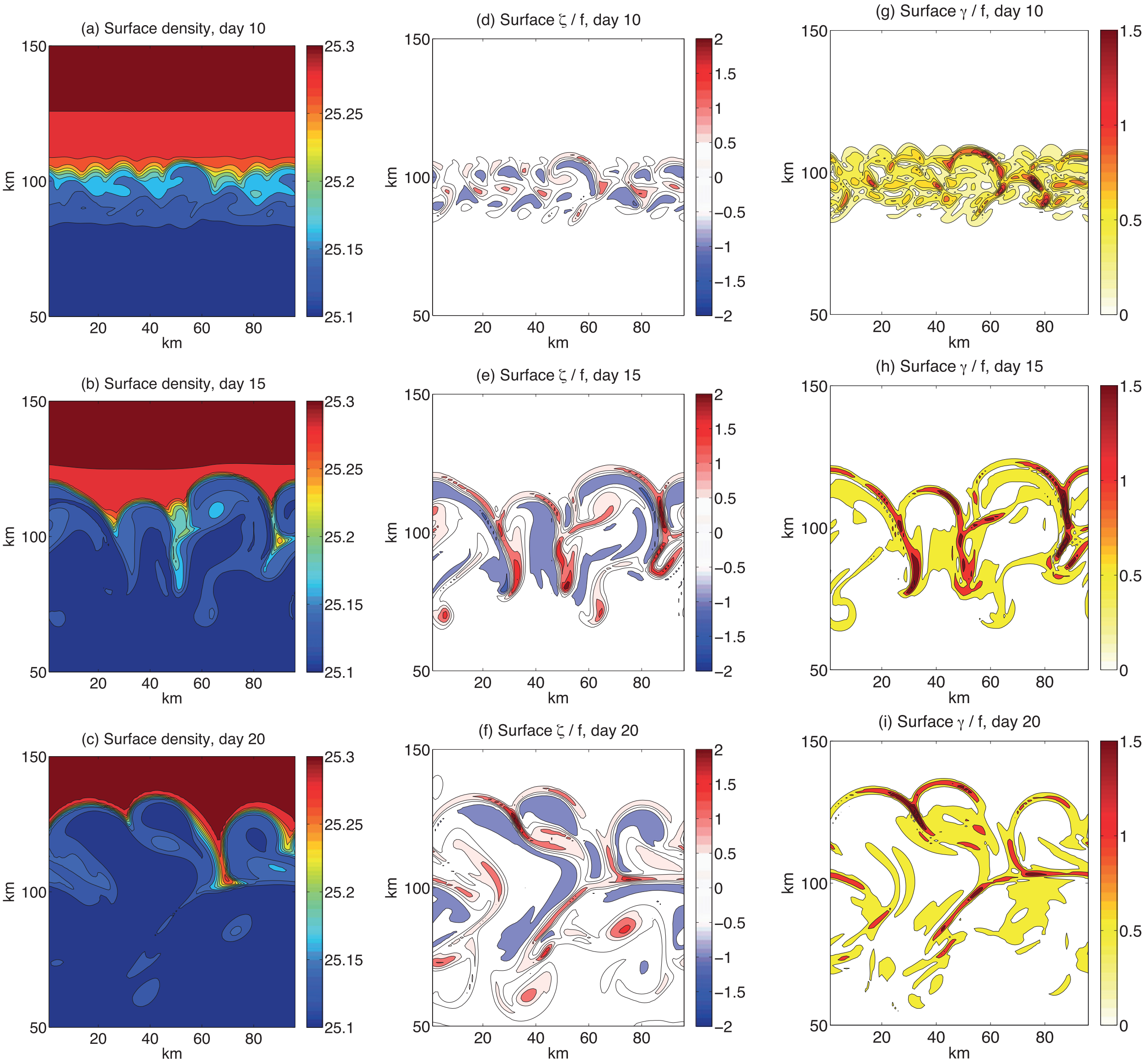

FIG. 1. The time evolution of ML instabilities is shown in terms of (a–c) surface density (sigma), (d–f) vertical component of the relative vorticity (ζ), and (g–i) horizontal strain rate γ, all plotted for the surface on days (top) 10, (middle) 15, and (bottom) 20 of the simulation. Here ζ and γ are normalized by f. The domain is 96 km (in x) × 192 km (in y); only the frontal region between y = 50 and 150 km is shown.

The *e*-folding depth of penetration for the ML eddies, according to (5), is $D \approx fL_s/N \approx (10^2\ \mathrm{m})$. The vertical structure of the ML eddies is, however, variable in time, with features progressively penetrating deeper into the pycnocline (Fig. 3c) despite the nonuniform stratification that acts to restrict the barotropization of the flow, at least in the quasi-geostrophic approximation (Smith and Vallis 2001). Theories to predict the correct vertical structure of the flow, such as surface quasi-geostrophy (SQG; e.g., Held et al. 1995; LaCasce and Mahadevan 2006) are based on N^2 being constant; here N^2 is not uniform in the vertical and varies in time because of the restratifying action of the ML eddies. Further work is required to explain the time evolution of the vertical structure of the instabilities.

b. Lateral dispersion of tracer

To study the along-isopycnal mixing of tracers in the pycnocline, we introduced tracer streaks beneath the ML front on isopycnal surfaces at varying depths as shown in Fig. 2. The time evolution of the tracer concentration along σ = 25.44 (Figs. 4a–c) shows that, under the action of ML instabilities, the tracer streak begins to form wiggles (as seen on day 10) that get stretched in the cross-front

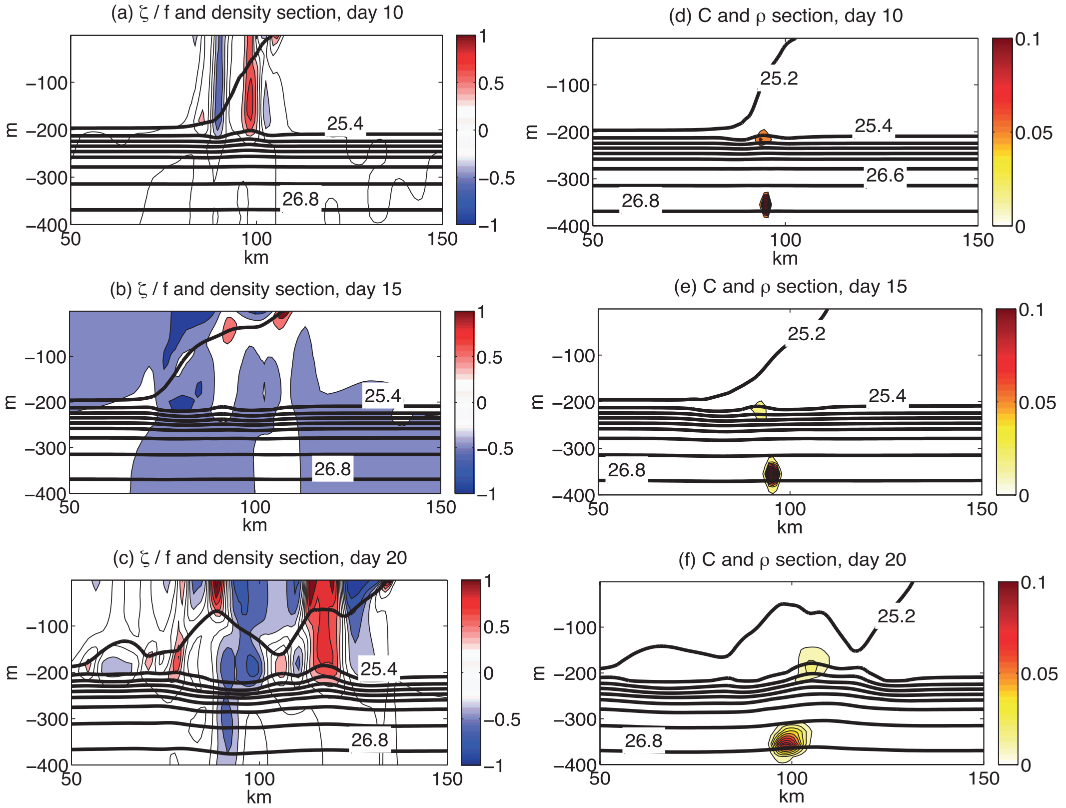

FIG. 2. (a–c) Vertical (y–z) sections of density (continuous bold lines) and relative vorticity ζ normalized by f (colors) along $x = 20$ km, and (d–f) vertical sections of density (continuous bold lines) and tracer concentration. Results are shown up to a depth of 400 m on days (top) 10, (middle) 15, and (bottom) 20 of the simulation.

direction. On day 15, the regions of high tracer concentration are linked to each other in a filament that is folding on itself (Fig. 4b). On day 20, we find that the previously continuous filament is broken into discrete blobs of tracer that evolve independently of each other (Fig. 4c). The time evolution of the maximum tracer concentration (Fig. 4a, insert) shows that for the first 3–5 days, the maximum tracer concentration does not change. Between days 5 and 15, the maximum tracer concentration decays rapidly and exponentially, following which, the decay rate slows considerably. At greater depths, along $\sigma = 26.76$, the tracer undergoes a similar evolution (Figs. 4d–f), but with a delayed response to the instabilities. At depth, the maximum tracer concentration decays at a slower rate and asymptotes toward a larger value than was reached on $\sigma = 25.44$.

Vertical sections of the tracer streaks taken along $x = 20$ km show that the tracer is mainly spreading along isopycnals (Figs. 2d–f). By day 20, the streak has spread from the initial position approximately 10 km in the horizontal direction and 100 m in the vertical direction. The ratio of the distribution of the tracer in the vertical to the horizontal direction gives a typical value of the tracer filament slope: $(\Delta C/\Delta z)/(\Delta C/\Delta y) = 10^2$. Taking a typical value of the buoyancy frequency in the interior of $N^2 = 10^{-4}\ \mathrm{s}^{-2}$, it is possible to see that $[(\Delta C/\Delta z)/(\Delta C/\Delta y)]^2 \sim N^2/f^2 = 10^4$, which is in agreement with the results of Haynes and Anglade (1997) and Smith and Ferrari (2009) for tracer filaments in the interior subject to both horizontal strain and vertical shear. Though we do not explore the role of vertical mixing in this study, Haynes and Anglade (1997) and Smith and Ferrari (2009) have shown that on account of the strong vertical shear that tilts filaments, even a small vertical diffusivity is sufficient to arrest the lateral downscale cascade of tracer variance.

The analysis of the tracer displacement from the center of mass shows that along $\sigma = 25.44$, the distribution is initially Gaussian. At later times, the tracer displacement shows significant deviation from the normal distribution (Figs. 5a–c). Analysis of the tracer displacement at the same time, but at greater depth [e.g., along $\sigma = 26.76$ (Fig. 5d)] and for the integrations with a decreased value of the cross-front density contrast $0.2b_{y0}$ (Fig. 5e) and initial ML depth $H = 100$ m (Fig. 5f), also show deviations from the Gaussian distribution, even if much less pronounced.

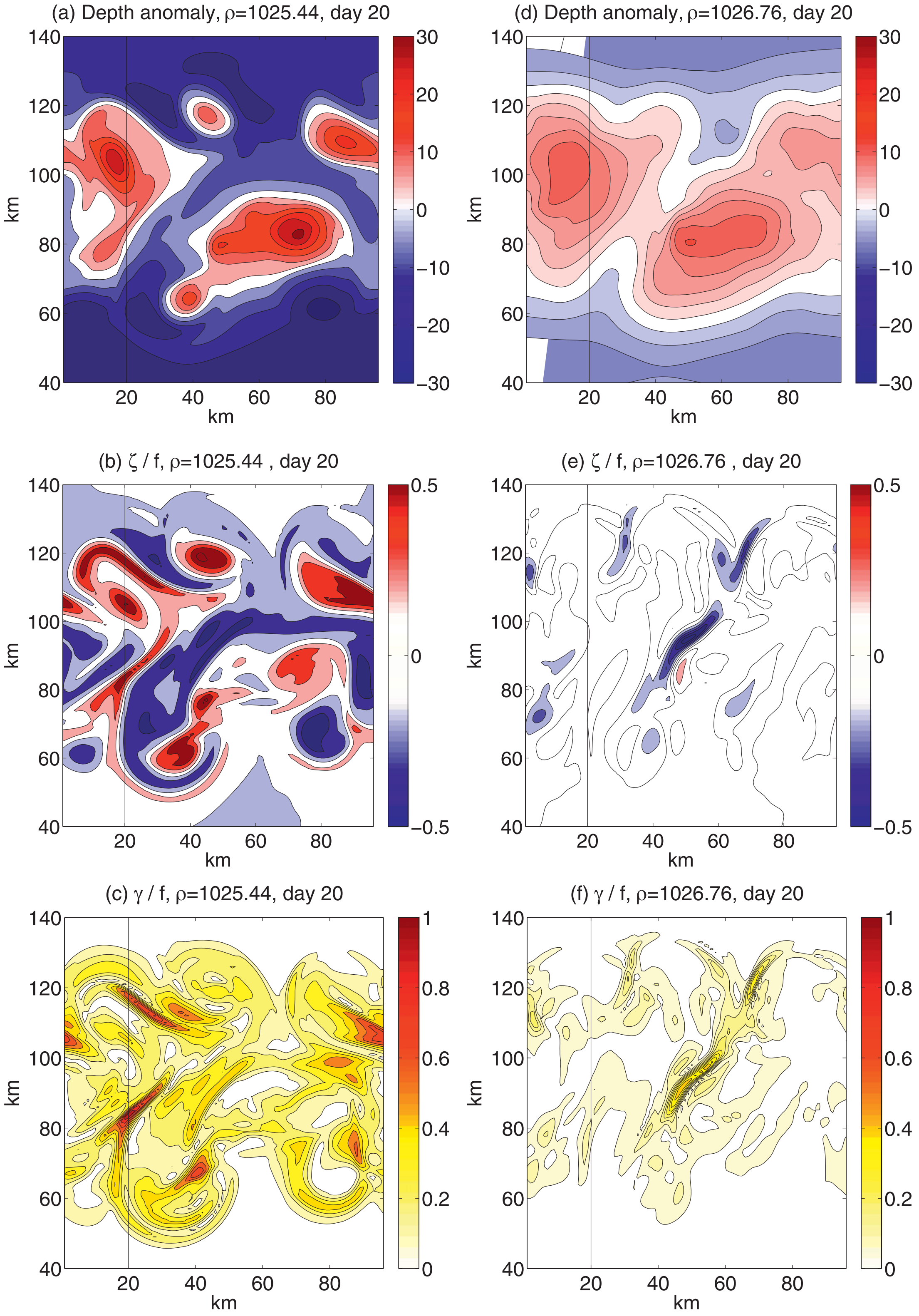

FIG. 3. Dynamical properties on day 20 of the simulation shown on a shallow and deep isopycnal surface in the pycnocline. (a) Depth anomaly (m), (b) relative vorticity ζ normalized by f, (c) lateral strain rate γ normalized by f along the isopycnal $\sigma = 25.44$; (d) depth anomaly (m), (e) ζ/f, and (f) γ/f along the isopycnal $\sigma = 26.76$. Black line at $x = 20$ km indicates the location of the vertical section in Fig. 2.

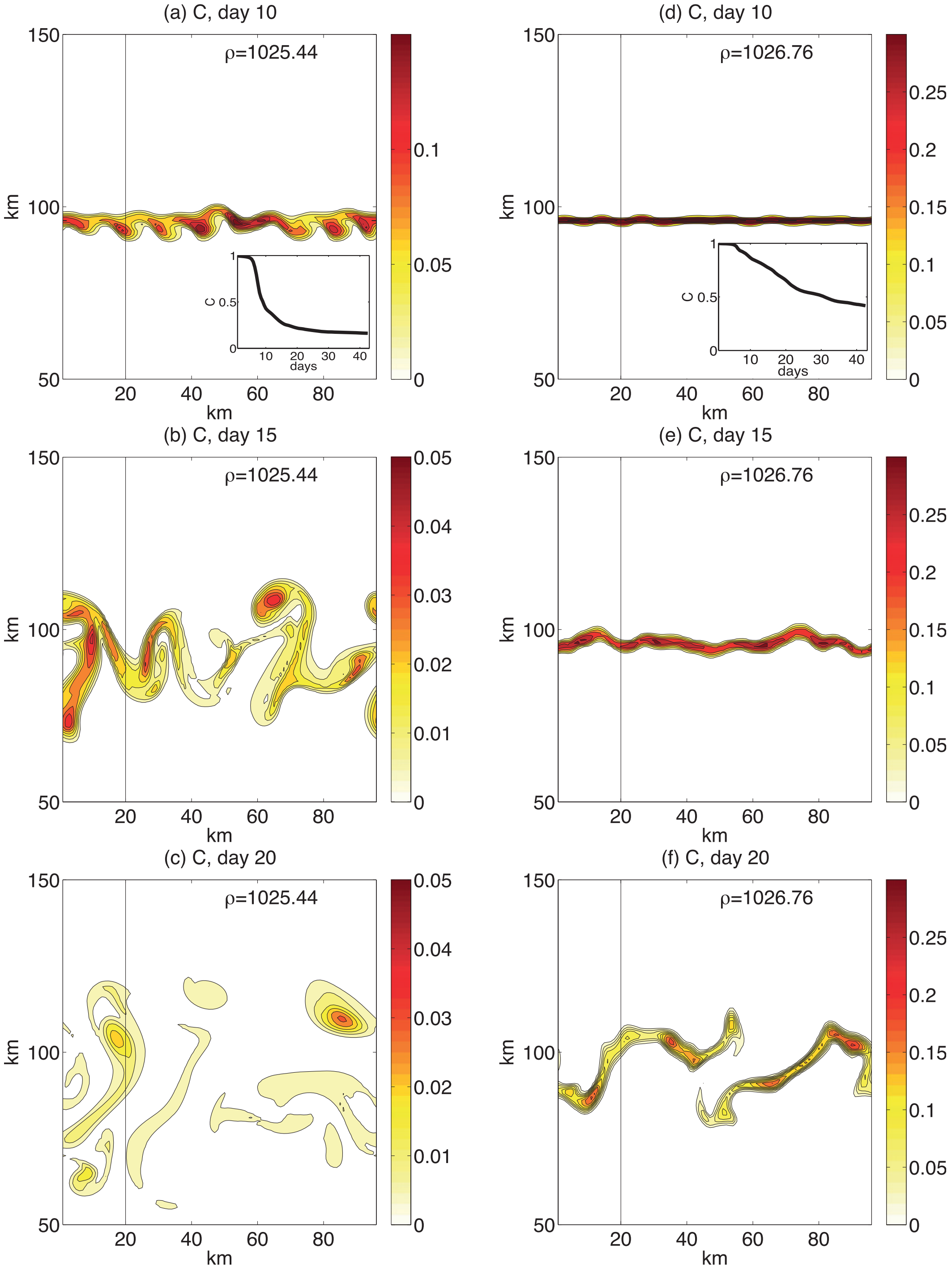

FIG. 4. Evolution of tracer concentration along (left) $\sigma = 25.44$ and (right) 26.76 for days (a),(d) 10, (b),(e) 15, and (c),(f) 20. Embedded in (a) and (d): time evolution of the maximum tracer concentration along (a) $\sigma = 25.44$ and (b) 26.76.

To analyze the dispersion of tracer by the eddying flow in the pycnocline, we estimate the tracer variance σ_{yy}, defined in (8), as a function of time. We find, as will be shown in the following analysis, that only at early times does the tracer behave diffusively. Thereafter, it gets caught in dynamic filaments with high strain rates, and gets rapidly stretched in the cross-front direction leading to an exponential growth in the variance. Consequently, a stage is reached when the tracer filaments break up, and the variance shows a power law behavior with time. A Fickian description for the tracer's behavior is thus valid only at early times.

A log–log plot of the time evolution of the tracer variance σ_{yy} (Fig. 6a) clearly shows the existence of three different dynamical regimes, as described below.

1) DIFFUSIVE REGIME

During the first 3–4 days, corresponding to about 6 inertial periods, the instabilities grow linearly and tracer dispersion increases linearly in time. In this period, the tracer variance evolves as $\sigma_{yy} \sim t^{1.1}$ (Fig. 6a). Around day 4, the evolution of tracer variance undergoes a sudden transition into the second regime.

2) EXPONENTIAL REGIME

From days 4 to 15, corresponding to 14 inertial periods, the tracer exhibits superdiffusive behavior, and the concentration variance grows as $\sigma_{yy} \sim t^{6.8}$ (Fig. 6a). In this period, tracer filaments are seen to show large excursions in y (Fig. 4b) and the growth of tracer filaments occurs at an exponential rate proportional to their strain rate (γ). To explain the rapid rate of increase in tracer variance by exponential growth of tracer filaments, we plot the time evolution of the tracer variance in semilogarithmic space (Fig. 6b). The exponential growth rate in this second, transient, regime suggests the presence of two-dimensional turbulence in the enstrophy cascade range (Lin 1972). Such exponential growth has been observed in the oceanic ML using tracers (J. Price 1981, unpublished manuscript) and surface drifters (Koszalka et al. 2009), and, subsurface of the Gulf Stream, using floats (LaCasce and Bower 2000).

Following Garrett (1983), (16) can be modified to include the effect of strain acting on the tracer streak as follows:

$$\sigma_{yy} = \pi \frac{K_y}{\langle\gamma\rangle} \exp\left[C_3\langle\gamma\rangle\left(t - \frac{1}{4\langle\gamma\rangle}\right)\right]. \qquad (23)$$

Here, $\langle\gamma\rangle$ is the ensemble strain rate acting on the tracer streak and C_3 is a constant of $O(1)$. While γ can be difficult to control because of the intermittency of the strain rate associated with filaments in both space and time, it is possible to create different numerical realizations that change $\langle\gamma\rangle$ through the deployment of tracers at different depths inside the pycnocline, or through a change of the initial parameters of the ML front as shown in Fig. 6c. We compare results from the upper and lower pycnocline for the reference integration (full and dashed lines in Figs. 6c,d), and in the upper pycnocline for a numerical integration with initial ML depth of 100 m. Figure 6d shows that the exponential growth rate (slope in semilogarithmic space) of the tracer variance for each of these cases varies with $\langle\gamma\rangle$ in accordance with (23). The deeper ML generates stronger filaments and larger $\langle\gamma\rangle$ (Fig. 6c) as expected based on the scaling for submesoscale flows in (4). Consequently, this case results in a higher growth rate of tracer variance (Fig. 6d). Similarly, because the EKE and strain rate decays with depth, the upper pycnocline has larger values of $\langle\gamma\rangle$ and shows higher growth rates.

3) RICHARDSON REGIME

From days 16 to 42 the tracer concentration variance along the isopycnal evolves as $\sigma_{yy} \sim t^{2.5}$ (Fig. 6a). In this period, the flow has attained finite amplitude instabilities. The tracer streak is broken into tracer blobs that evolve independently (Fig. 4c).

The time evolution of the tracer variance suggests the presence of two-dimensional turbulence in the inverse energy cascade range with -3 slope in the KE spectrum. The power law dependence of tracer variance in the third regime is in agreement with upper-ML observations by (Okubo 1971), which reported $\sigma_{yy} \sim t^{2.3}$. The transition time between the second and the third regime is in agreement with the observations of surface floats by Koszalka et al. (2009).

Analysis of the time evolution of the KE spectra (Fig. 7a) shows the initial excitation of the kinetic energy on the $\approx$10 km scale and the subsequent nonlinear cascade to larger scale. Analysis of the KE spectrum at day 41 (Fig. 7b) shows the presence of $k^{-5/3}$ slope at synoptic scales and k^{-3} slope at smaller scales, confirming the presence of an inverse energy cascade range and an enstrophy cascade range. At even smaller scales, the spectra become steeper because of the action of viscosity. The slope of the spectra is the same along different isopycnals at different depths.

To test the sensitivity of the results to the initial tracer distribution, we performed experiments where the tracer streak width was given an initial Gaussian distribution over 10 km (10 grid cells) and a maximum concentration of 1 unit. Results do not differ from those obtained with the 1-km-wide streak; we see the presence of the three regimes and the first regime shows the same time dependence in σ_{yy}. Also, the sensitivity of our results to the numerical parameters in the model was tested by reducing both horizontal momentum viscosity and horizontal tracer diffusivity to $\nu_h = 1\ \mathrm{m^2\ s^{-1}}$ and $\kappa_H = 1\ \mathrm{m^2\ s^{-1}}$. Again, for the first regime, the slope of the tracer variance is the same as the value found for the larger values of horizontal diffusivity and viscosity, implying that our results do not depend on the specific choice of these model parameters.

It is of interest to estimate a lateral diffusivity for the tracer as a measure of mixing, but, since the tracer variance shows non-Fickian behavior in this regime, it

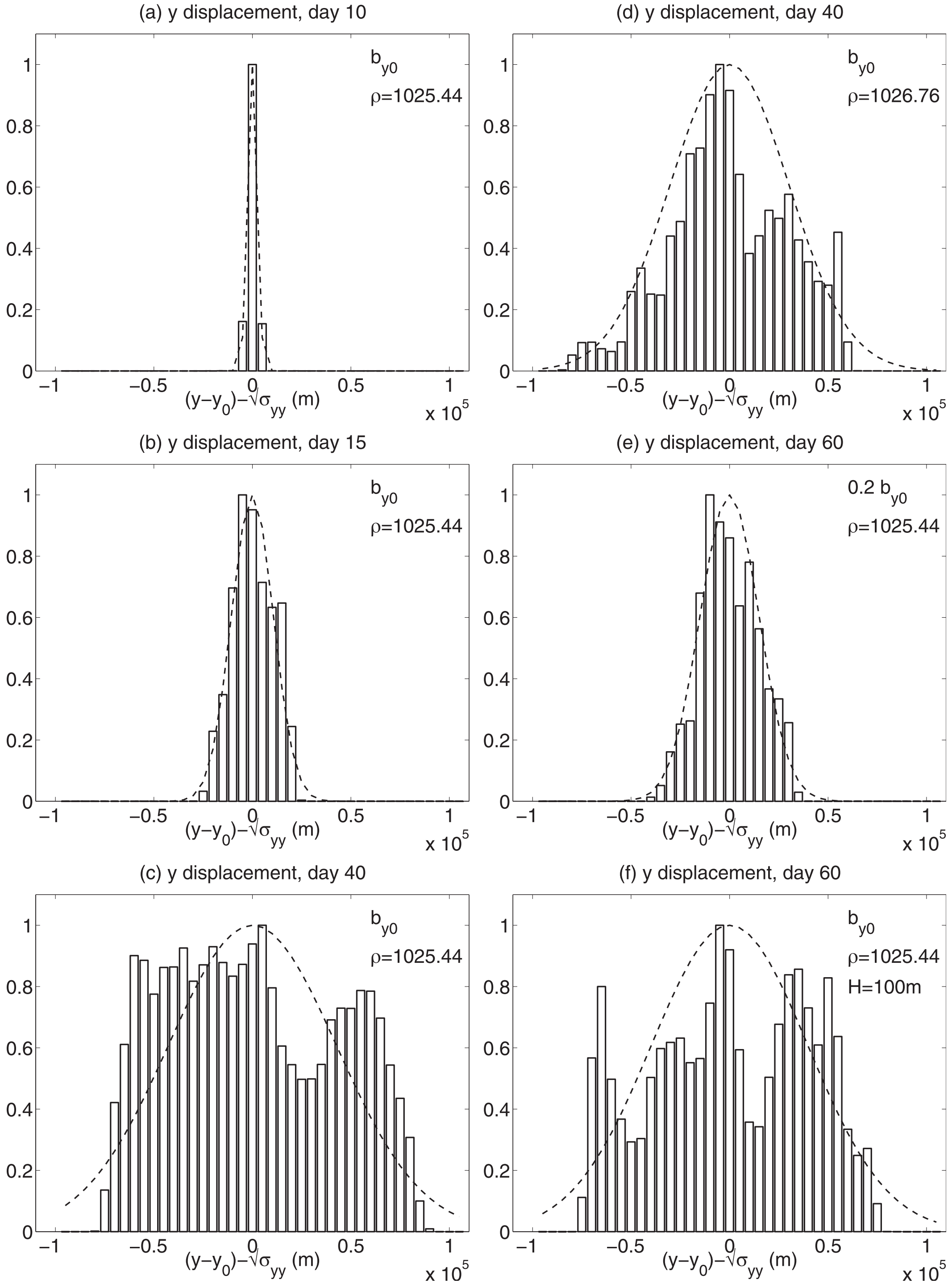

FIG. 5. Normalized histograms of quantity of tracer in function of the meridional displacement (m) of the tracer from its center of mass, $(y - y_0) - \sqrt{\sigma_{yy}}$, where y_0 is the meridional position of the center of the domain. (left) Results from the reference integration along $\sigma = 25.44$ for days (a) 10, (b) 15, and (c) 40, representing the first, second, and third regime, respectively. (right) We show (d) the reference integration at day 40, along $\sigma = 26.76$; (e) the integration with b_{y0} diminished to $0.2b_{y0}$ at day 60; and (f) the integration with initial ML depth decreased to $H = 100$ m at day 60. Dashed lines represent the Gaussian distribution with standard deviation calculated from the tracer variance. Non-Fickian dispersion in the second and third regime leads to a deviation from the Gaussian distribution that is expected of a diffusive process. The non-Fickian behavior sets in at later times on deeper isopycnals and when the submesoscale ML eddies are weaker (i.e., for smaller H and b_y).

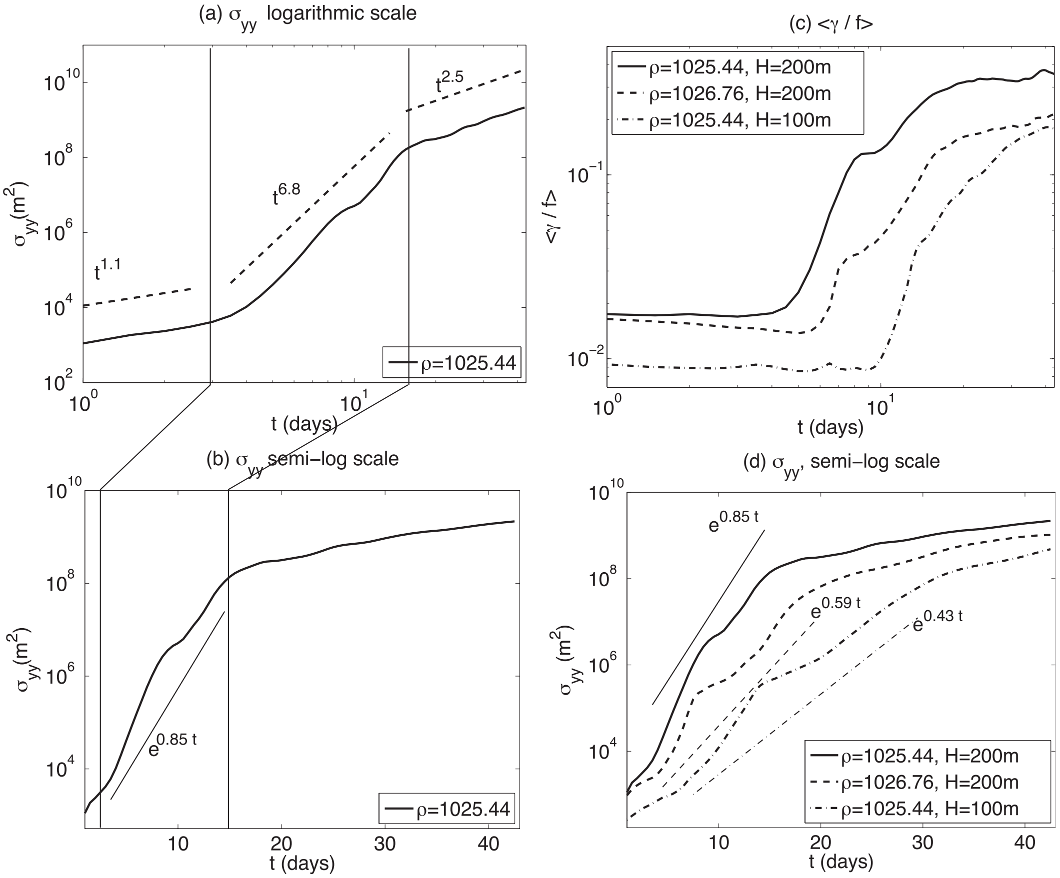

FIG. 6. Time evolution of the tracer concentration variance σ_{yy} along $\sigma = 25.44$ plotted on (a) logarithmic and (b) semilogarithmic scales. (c) Time evolution of the area-averaged strain rate (normalized by f) $\langle\gamma/f\rangle$ on different isopycnals (shallow and deep) and with ML $H = 100$ m (for the shallow isopycnal). The evolution of the strain rate also exhibits a transition from one regime to another, but remains consistently higher for the shallower isopycnal and the simulation with deeper mixed layer. (d) Time evolution of the tracer concentration variance along $\sigma = 25.44$ (bold line) and along $\sigma = 26.76$ (dashed line) for the reference integration, and along $\sigma = 25.44$ for the numerical integration with initial ML depth of 100 m (dotted-dashed line). In (a), we find three distinct regimes characterized by $\sigma_y^2 \sim t^{1.1}, t^{6.8}$, and $t^{2.5}$. In (b) and (d) we find that the second regime is near exponential. Thin straight lines represent linear fits to estimate the exponential growth rate in the second dynamical regime.

would not be appropriate to assume a constant lateral diffusivity for the tracer according to (15). Instead, we examine the time-dependent, apparent diffusivity (K_a), expressed in accordance with Richardson (1926) and Okubo (1971) as

$$K_a(t) = \frac{\sigma_{yy}}{4t}. \qquad (24)$$

For Fickian diffusion, K_a would be constant and equivalent to K_y in (15) (Einstein 1905; Taylor 1921). Using a wide range of observations, Okubo (1971) showed that K_a varies with the diffusive length scale (Λ) defined (for dispersion in the y direction) as

$$\Lambda = 3\sqrt{\sigma_{yy}}. \qquad (25)$$

This definition of Λ is based on the fact that if the tracer has a Gaussian distribution in the meridional direction, most of the tracer will be contained within $3\sqrt{\sigma_{yy}}$. The time evolution of K_a and Λ (Fig. 8a) shows that both quantities covary in time, and both exhibit the three dynamical regimes noted for σ_{yy}. However, initially, the dispersive length scale $3\sqrt{\sigma_{yy}}$ is smaller than what can be resolved by the model, and Λ and K_a are meaningful only at later times (i.e., in the third regime). Plotting K_a versus Λ for the third regime (Fig. 8b) reveals that the modeled tracer shows the behavior

$$K_a \sim \Lambda^{1.24}. \qquad (26)$$

This 1.24 power dependence inferred for the model simulations is higher than the value of 1.1 obtained from observations by Okubo (1971), but lower than the

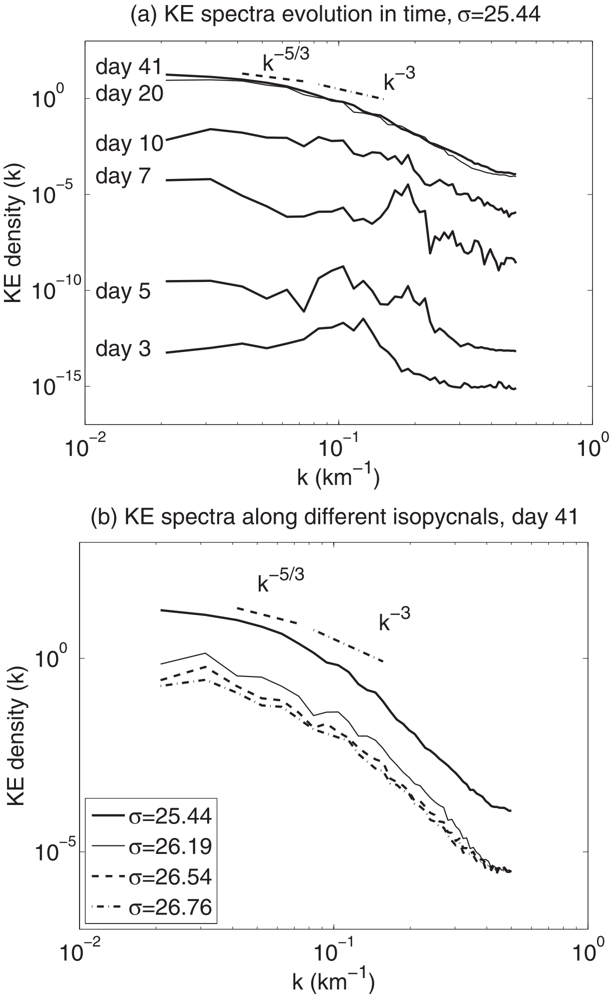

FIG. 7. (a) Time evolution of the kinetic energy spectra along $\sigma = 26.76$ for the reference integration. (b) Kinetic energy spectra at day 41 for the reference integration along $\sigma = 25.44$ (full bold line), 26.19 (full thin line), 26.54 (dashed line), and 26.76 (dotted-dashed line).

4⁄3 Richardson power law in (19) that is proposed to hold in the ocean (Stommel 1949; Ollitrault et al. 2005; Lumpkin and Elipot 2010).

We make a further effort to estimate a time-dependent horizontal diffusivity K_y as a measure of lateral mixing by using each of the three proposed relationships (15), (17), and (19) within each of the three regimes. To do this, we must first estimate the transition times between the diffusive and exponential regimes and between the exponential and Richardson regime. In particular, the transition time between the diffusive and exponential regimes can be calculated from (15) to (17) as

$$t_{1,2} = \frac{1}{4}\frac{1}{C_1\eta^{1/3}}, \qquad (27)$$

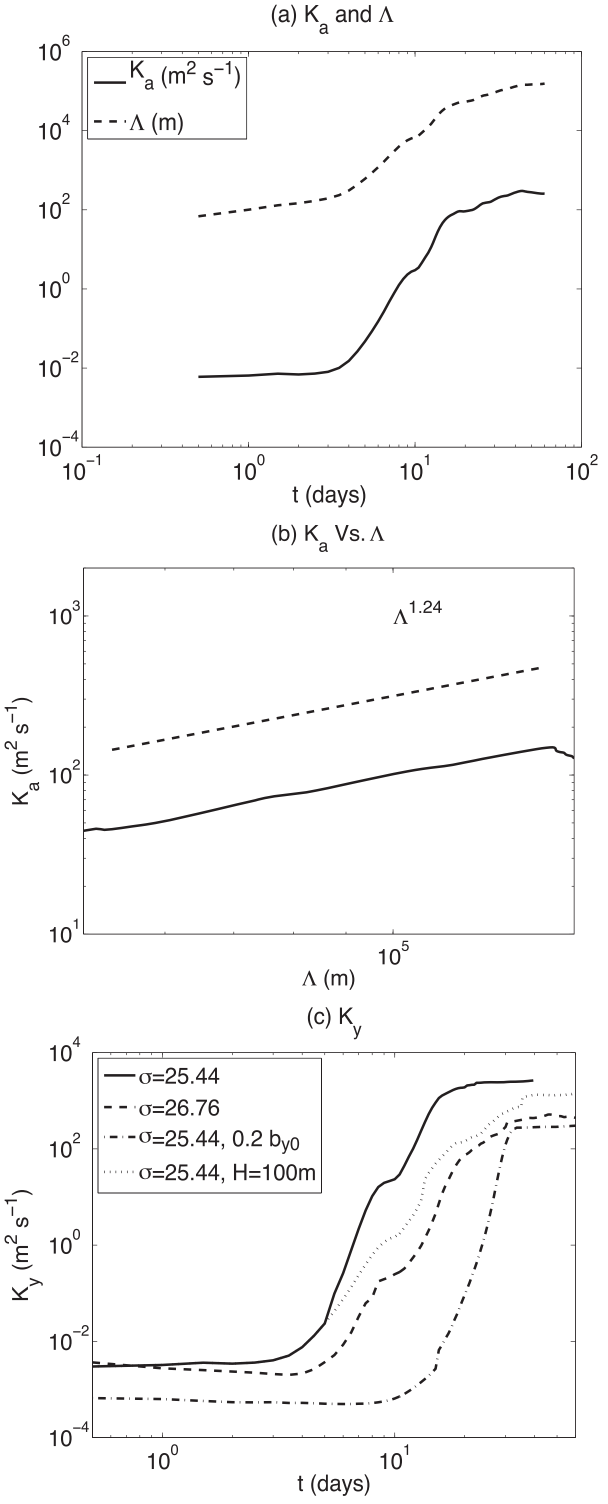

FIG. 8. (a) Evolution in time of the apparent diffusivity K_a (m^2 s^{-1}) (full line) and diffusive length Λ (m) (dashed line). (b) Plot of the apparent diffusivity vs the diffusive length for the third regime. (c) Evolution in time of the lateral diffusivity K_y (m^2 s^{-1}) along $\sigma = 25.44$ (full line) and 26.76 (dashed line) for the reference integration, along $\sigma = 25.44$ for the integration with initial b_y set as $0.2b_{y0}$ (dotted-dashed line), and along $\sigma = 25.44$ for the integration with initial ML depth $H = 100$ m (dotted line).

where the constant C_1 can be found from linear regression from the reference integration. The transition time between the exponential and Richardson regime ($t_{2,3}$) has no simple analytical form and is thus estimated from the transition in the rate of increase in variance.

We then calculate K_y in each of the three regimes using (15), (17), and (19), respectively, having estimated η and ϵ—the enstrophy and energy dissipation rates. The resulting K_y is shown in Fig. 8c for different model simulations. For the reference integration (full line), during the first regime K_y has the value of 10^{-2} m^2 s^{-1}. During the second regime K_y increases to approximately 2300 m^2 s^{-1}. Finally, during the third regime, the growth rate of K_y decreases. By the end of the integration, K_y reaches the value of approximately 2500 m^2 s^{-1}. We see a strong dependence of K_y on the depth of the isopycnal along which the tracer is released (dashed line), the lateral buoyancy gradient in the ML b_y (dotted-dashed line), and on the initial ML depth, H (dotted line). The exact scaling dependence is, however, not clear. In general, results can be influenced by the relationship between the depth of the isopycnal on which K_y is calculated and the value of N^2 in the pycnocline. In fact, changes of the initial ML depth H also result in changes in N^2, and these can affect the penetration depth of the ML eddies and then can affect the lateral mixing.

Analysis of the tracer variance at different depths and for different initial values H and b_y (given in Table 2) show that the various simulations differ in the rate of growth of tracer variance. But, the presence of the three turbulent regimes described in section 4b, and the 1.24 power law between apparent diffusivity (K_a) and the diffusion scale (Λ) are robust for all the cases.

Since these numerical experiments were started from an idealized initialization of a front, one may ask how these analyses might apply when tracer is introduced in a flow field that has already spun up, as when dye is injected in the ocean. To address this question, we injected the tracer streaks at 10 and 20 days after model initialization. Our results, shown in Fig. 9, reveal that the tracer variance grows very abruptly when the tracer is introduced, so that within a short period it catches up to the level that it would have attained had the tracer been introduced at the beginning of the model integration.

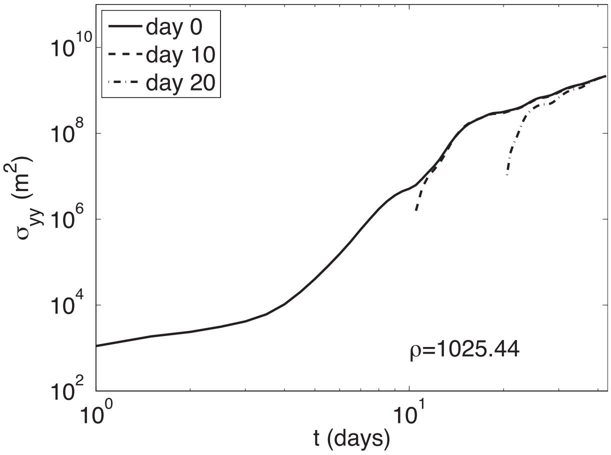

FIG. 9. Evolution in time of the tracer variance σ_{yy} (m^2) along σ = 25.44 for tracer deployed in a streak at the beginning of the numerical integration (full line) at days 10 (dashed line) and 20 (dotted-dashed line).

c. *Comparison with other mechanisms for horizontal mixing*

The values found for K_y can be compared with the values found from other mechanisms for horizontal mixing acting in the oceanic pycnocline. Holmes-Cerfon et al. (2011) calculated the horizontal particle dispersion due to random waves in a three-dimensional rotating and stratified Boussinesq system, which acts as an idealized model for tracer dispersion in the ocean by the internal wave field. Using the parameters utilized in our study, the single-particle diffusivity [Holmes-Cerfon et al. 2011, their Eq. (8.6)] leads to a horizontal diffusivity for the Garrett–Munk (e.g., Munk 1981) internal wave spectra of $K_y \approx 0.12$ m^2 s^{-1}, which is an order of magnitude larger than the diffusivity induced by ML eddies in the pycnocline during the first regime. The diffusivity found by Holmes-Cerfon et al. (2011) is, however, limited by the fact that it is based on one-particle dispersion. Multiple-particle dispersion is expected to give larger values for the interior horizontal diffusivity induced by internal waves. Our values for K_y are also compared with the horizontal diffusivity due to internal wave shear dispersion. Using the relationship found by Young et al. (1982) for internal wave shear dispersion with parameter values used in this study, we estimate $K_y \approx 0.04$ m^2 s^{-1}, which is a factor of three lower than the single-particle dispersion estimate Holmes-Cerfon et al. (2011), but comparable or larger than our estimate for interior diffusivity by ML eddies during the first regime. Finally, our values for K_y can also be compared with the horizontal diffusivity due to vortical modes generated from the adjustment of mixed patches following diapycnal mixing events. Using the relationship for K_y in Sundermeyer and Lelong (2005), their Eq. (9), along with parameter values used in our study gives $K_y \approx 2$ m^2 s^{-1}, which is larger than internal wave-driven mixing and the value of interior diffusivity generated by ML eddies in the first regime within this study. At early times in the development of ML eddies (i.e., within the first regime), it would be difficult to distinguish the effect of ML eddies on mixing in the pycnocline from other mechanisms. But, when developed (i.e., in regimes 2 or 3), ML eddies provide a distinct enhancement in mixing, far beyond what can be achieved by other mechanisms like internal waves and vortical modes.

d. Effective diffusivity of filaments

To better understand the role of singular submesoscale filaments in lateral mixing, we use a tracer that was initialized on an isopycnal surface with a uniform gradient in y. To isolate the effect of submesoscale filaments, we use the simulation with a fivefold stronger lateral buoyancy gradient ($b_y = 5b_{y0}$), which produces pronounced filaments. Figure 10a shows the tracer concentration on day 18 of the integration. We focus, hereafter, on a subdomain (Fig. 10b) containing a distinct filament that exhibits high relative vorticity (ζ; Fig. 10c), strain rate (γ; Fig. 10d), and potential vorticity (Fig. 10e). Both ζ and γ exceed f, highlighting the submesoscale character (Mahadevan and Tandon 2006) of the filament.

The quantity K_{eff} is estimated using (21) and (22) and shown in Fig. 11a. Surprisingly, the filament, which is instrumental in rapidly enhancing the dispersion of tracer, is delineated by a region of zero K_{eff} at the filament center, with $K_{\text{eff}} \approx 600\ \text{m}^2\ \text{s}^{-1}$ on the edges. Its effect on tracer fluxes becomes apparent when we examine the lateral tracer flux $K_{\text{eff}} \cdot \nabla C$ in Fig. 11b. Enhanced fluxes are found along the filament boundary. To test the dependence of the barrier behavior of filaments on numerical parameters, the model was integrated with $\nu_h = 1\ \text{m}^2\ \text{s}^{-1}$ and $\kappa_H = 1\ \text{m}^2\ \text{s}^{-1}$. Results (not shown) show the presence of filaments with zero K_{eff} at the filament center and with enhanced fluxes are found along the filament boundary, thus suggesting the independence of the result to model parameters.

The region of zero effective diffusivity in the core of the filament suggests that the filament is a barrier to mixing in its interior and must therefore carry tracer without mixing it in its core, but eventually exchange it with the surrounding region across its edges. This behavior is different from that of mixing barriers associated with open-ocean jets, where mixing is suppressed by the mean flow (Marshall et al. 2006; Smith and Marshall 2009; Abernathey et al. 2010; Ferrari and Nikurashin 2010). In submesoscale filaments, the mechanism generating zero K_{eff} in the filament is horizontal shear, which acts to move the tracer contours parallel one to each other without deforming them. The hypothesis that the center of the filament is dominated by shear flow is supported by the observation that it contains both high-vorticity and high-strain rate at the same location. Figure 10f shows the horizontal shear, calculated as

$$\alpha = \frac{|[\hat{z} \times \mathbf{u}] \cdot \nabla \mathbf{u}|}{|\mathbf{u}|}, \tag{28}$$

to be enhanced in the core of the filament. However, shear flows also exhibit diffusion in the form of Taylor dispersion (Taylor 1953), which acts along the tracer concentration contours rather than across them.

For an idealized 2D tracer filament balanced by the action of horizontal strain γ in the x direction and horizontal diffusivity κ_H, the advection–diffusion equation can be written as

$$\frac{\partial C}{\partial t} + \gamma x \frac{\partial C}{\partial x} - \gamma y \frac{\partial C}{\partial y} = \kappa_H \left(\frac{\partial^2 C}{\partial x^2} + \frac{\partial^2 C}{\partial y^2} \right). \tag{29}$$

Assuming a balance between the along-filament strain and the across-filament diffusivity, (29) predicts a typical filament width (Garrett 1983)

$$W \sim \sqrt{\frac{\kappa_H}{\gamma}}. \tag{30}$$

For $\kappa_H = 5\ \text{m}^2\ \text{s}^{-1}$ and $\gamma = O(f)$, (30) yields $W \approx 200$ m. However, the strong horizontal shear implies that Taylor dispersion can also contribute to filament lengthening. Assuming $\mathbf{u}_H = \gamma x + U_0[(1 - y^2/W^2)]\hat{x}$, where y is now the cross-filament coordinate with respect to the filament center about which the flow is assumed axisymmetric and U_0 is a typical along-filament velocity, after a Reynolds decomposition, (29) yields (Taylor 1953)

$$\begin{aligned} \frac{\partial C}{\partial t} + \gamma x \frac{\partial C}{\partial x} - \gamma y \frac{\partial C}{\partial y} = \kappa_H \left[1 + \mu W^2 \frac{(\gamma x)^2}{\kappa_H^2} \right] \frac{\partial^2 C}{\partial x^2} \\ + \kappa_H \frac{\partial^2 C}{\partial y^2}, \end{aligned} \tag{31}$$

where μ is a nondimensional constant of order 1. The Taylor dispersion term enhances the effect of the horizontal strain in elongating the filament. Assuming $W^2[(\gamma^{L_f})^2/\kappa_H^2]W^2 \gg 1$, where L_f is the typical length of the filament, for $\kappa_H = 5\ \text{m}^2\ \text{s}^{-1}$ and $\gamma = O(f)$ the Taylor dispersion and the horizontal diffusivity terms are both of $O(10^{-4}\ \text{C})$. The balance between Taylor dispersion and the horizontal diffusivity gives $W^2\gamma^2/\kappa_H \sim \kappa_H/W^2$, which results in the same balance as (30). Along-filament Taylor dispersion resulting from the large lateral shear in filaments can thus have a similar contribution as the lateral strain rate in elongating tracer filaments. Its neglect could thus lead to an overestimation in the width of the tracer filaments.

The order of magnitude of K_{eff} is in agreement with the relationship between the Nusselt number $Nu = K_{\text{eff}}/\kappa_H$

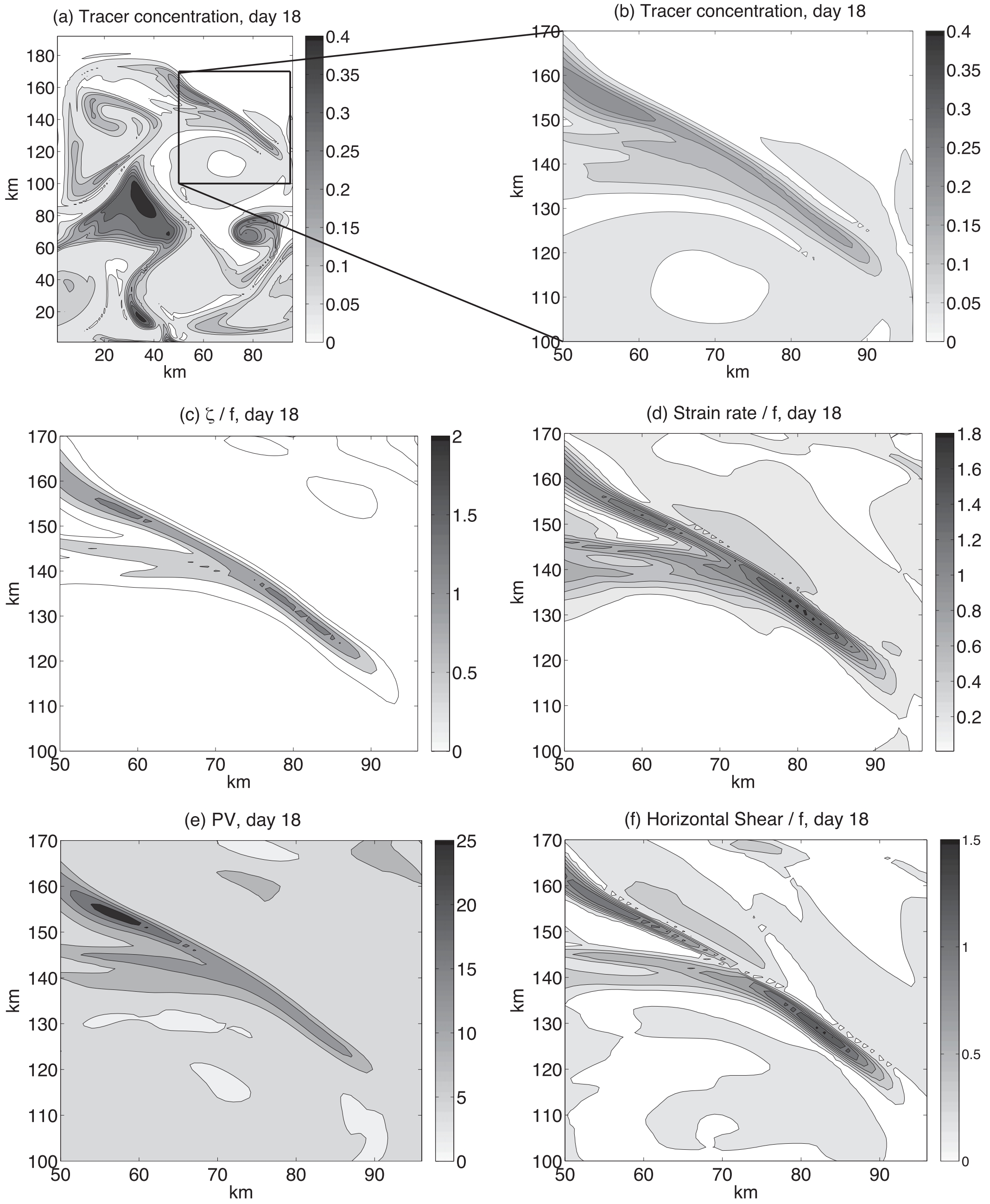

FIG. 10. (a) Tracer concentration for the entire domain along $\sigma = 25.44$ at day 18 for the $5b_{y0}$ integration. The following focus on a subregion: (b) tracer concentration, (c) relative vorticity (ζ) normalized by f, (d) lateral strain rate (γ) normalized by f, (e) potential vorticity (10^{-9} m^{-1} s^{-1}), and (f) horizontal shear normalized by f for a submesoscale filament forming in the pycnocline.

and the Peclet number $\mathrm{Pe} = UL/\kappa_H$ of the flow (Shuckburgh and Haynes 2003; Marshall et al. 2006). For a filament (Fig. 10a) with typical velocity of $O(1\ \mathrm{m\ s^{-1}})$ and typical cross-filament size of $O(10\ \mathrm{km})$, $\mathrm{Pe} = O(10^2)$, which corresponds to $Nu = K_{\mathrm{eff}}/\kappa_H = O(10^2)$. The value of Pe found through the simple scaling suggests that the flow is in a regime in which K_{eff} is independent of κ_H (Shuckburgh and Haynes 2003; Marshall et al. 2006).

5. Discussion

Previous work has examined submesoscale instabilities within the mixed layer and their role in the vertical

(a) K_{eff} day 18

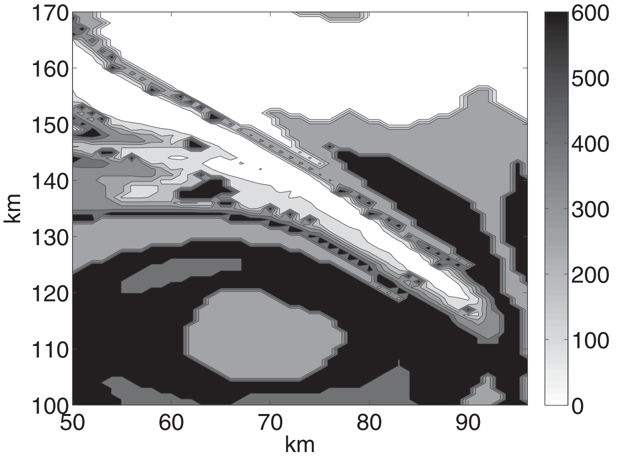

(b) $K_{\mathrm{eff}} \cdot \nabla c$ day 18

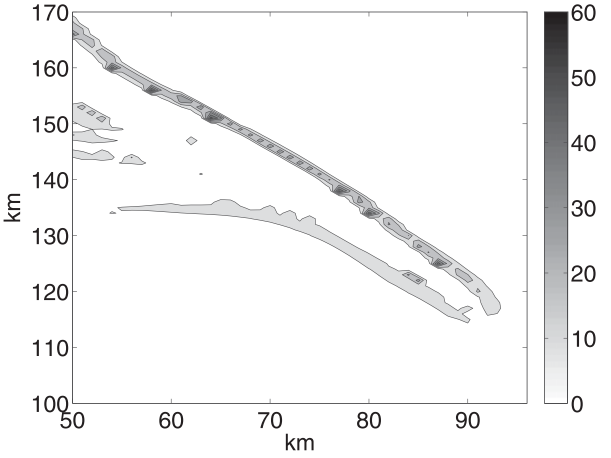

FIG. 11. (a) Effective diffusivity ($\mathrm{m^2\,s^{-1}}$) and (b) lateral tracer flux along isotracer lines ($\mathrm{m\,s^{-1}}$) for a submesoscale filament forming in the pycnocline along $\sigma = 25.44$ at day 18 for the $5b_{y0}$ integration.

exchange of properties between the surface and pycnocline. Lateral mixing in the pycnocline had been hypothesized to result from interior processes like vortical modes (Kunze 2001), resulting from internal wave induced mixing. Here, we show that surface-intensified processes in the mixed layer also generate significant lateral mixing in the interior. Current ML eddy parameterizations (Fox-Kemper et al. 2008) are designed to represent the effect of ML eddies within the surface ML. Our findings suggest that such parameterizations may also need to account for the effect of ML eddies in the pycnocline.

Observational studies of mixing in the pycnocline have used dye dispersion (Ledwell et al. 1998; Sundermeyer and Ledwell 2001) to quantify lateral mixing in terms of a horizontal Fickian diffusivity. But in our numerical experiments, the action of ML eddies results in a nonconstant lateral diffusivity in the pycnocline that cannot be represented by Fickian diffusion, except at early times.

Filaments that are generated by the mesoscale strain field have been known to have an effect on tracers. In a 2D mesoscale flow field, the cross-filament diffusion of tracer has been conjectured to arrest the elongation of the filament due to strain (Garrett 1983). In 3D, vertical diffusion comes into play on account of the strong vertical shear, and arrests filamentation (Haynes 2001; Smith and Ferrari 2009). Here, we examine submesoscale filaments, in which both the horizontal shear and strain rate are of the same order. For such filaments, Taylor dispersion arising from horizontal shear could enhance the growth of the filament. Our scaling analysis suggests that it may be important to consider the horizontal shear, in addition to the lateral strain rate, in estimating the cross-filament diffusivity.

Finally, the processes described here are likely to play a role in the distribution and fluxes of biogeochemical properties in the upper ocean. Even though the biogeochemical sources and sinks for nitrate are patchy, the correlation between density and nutrient is generally very robust in the pycnocline (e.g., Kamykowski and Zentara 1986). The dynamics described here may be of importance in homogenizing properties, such as nutrients, along isopycnals.

6. Conclusions

A series of numerical simulations were conducted to isolate the effect of ML eddies on the lateral mixing of tracers in the ocean interior. Our results show the importance of ML processes in influencing the dynamics and the mixing in the pycnocline. The strength of along-isopycnal lateral mixing is highly variable and dependent on parameters like the ML depth and lateral buoyancy gradient in the ML, as well as the isopycnal depth and vertical buoyancy gradient within the pycnocline. The evolution of tracer streaks injected in the pycnocline shows the presence of three distinct turbulent regimes characterized by differences in the growth of the dispersion. Initially, there is a diffusive regime where dispersion increases linearly in time. This is followed by a period in which the tracer experiences an exponential growth in the dispersion because of the integrated action of strain. Finally, the fully developed flow exhibits a Richardson-like power law in the growth of dispersion. The tracer variance is found to exhibit these three regimes for a wide range of model parameters (H and b_y) and isopycnal surfaces on which dye is released. The time-varying lateral diffusivity (K_y) consequently reflects the three dynamical regimes and a dependence on the submesoscale parameters, depth of isopycnal, and background stratification in the pycnocline. Submesoscale filaments that are characterized by the coincidence of large horizontal strain rate and vertical vorticity act to rapidly flux the tracer and increase tracer dispersion. However, the Nakamura effective diffusivity is small in the core of the filaments. The horizontal shear in the filaments overwhelms cross-frontal diffusion and filament centers act as barriers to transport, while eddy fluxes are enhanced only at the filament edges where tracer gradients are largest.

Acknowledgments. The authors thank Prof. Jean-Luc Thiffeault for helpful discussions. Constructive comments from two anonymous referees strengthened the manuscript. The authors are thankful to ONR (Awards N00014-09-1-0179 and N00014-09-1-0196) for support. This study is a part of the ONR Departmental Research Initiative "Scalable Lateral Mixing and Coherent Turbulence."

APPENDIX

Model Description

The model is an extension of the three-dimensional, nonhydrostatic, free-surface model described in Mahadevan et al. (1996a,b, 2010). Model parameters are summarized in Table 1. The model is set up in a zonally periodic channel with impermeable vertical walls at the meridional boundaries and at the bottom. The horizontal dimensions are $L_y = 192$ km in the meridional direction, $L_x = 96$ km in the zonal direction, and $H_{\text{tot}} =$ 500-m depth. The horizontal resolution is 1 km. In the vertical the model has 32 layers, but the vertical resolution is variable with depth, with enhanced resolution of 2 m near the sea surface, decreasing to the resolution of 36 m at depth. Lateral free-slip boundary conditions are applied. The model is nonhydrostatic, even though the instabilities described are hydrostatic (Mahadevan 2006). The domain is initialized with a sharp lateral north–south density gradient in the upper layers, with isopycnals initially vertical. The southern half of the domain has lighter water, and is initialized using an analytic profile of the form $\Delta\rho = \Delta\rho \tanh[0.03\pi(y - L_y/2)]$, which describes a surface ML front centered at 80 km north of the southern boundary. In the reference integration, the front has an initial cross-front density contrast of $\Delta\rho_0 = 0.2$ kg m^{-3} and an initial cross-front buoyancy gradient of $b_{y0} = -0.9 \times 10^{-7}$ s^{-2}. The initial depth of the ML is $H = 200$ m and the initial ML buoyancy frequency is $N^2 = 10^{-6}$ s^{-2}. The ML front is in thermal wind balance, with the level of no motion set at the top of pycnocline where the isopycnals are initially flat, so that initially no mean flow penetrates into the stratified region underlying the ML. The underlying pycnocline has been initialized from a typical density profile from the North Atlantic taken from the *World Ocean Atlas* (Levitus 1982). Initially, the pycnocline is flat, with nonuniform stratification with an initial maximum value of $N^2 = 1.8 \times 10^{-4}$ s^{-2} at 240 m and decreasing to $N^2 = 10^{-5}$ s^{-2} at 500 m, which is in general agreement with open-ocean values (e.g., Lewis et al. 1986; Planas et al. 1999). For comparison, some of the numerical simulations of the upwelling fronts generated in the California Current system by Capet et al. (2008b), their Figs. 5 and 10, have a slightly larger value of $b_y \approx -1.3 \times 10^{-7}$ s^{-2} and smaller initial ML depth $H \approx 50$ m.

The model is initialized with different values of lateral buoyancy gradient $0.2b_{y0}$, $0.5b_{y0}$, $0.75b_{y0}$, and $5b_{y0}$. The numerical integration with reference cross-front buoyancy gradient of b_{y0} is also integrated with an initial ML depth $H = 100$ and 150 m. Changes in ML depth result in changes to N^2 at the base of the ML, as the ML base matches the pycnocline at different depths corresponding to different buoyancy frequencies. All the numerical experiments performed are summarized in Table 2. The model has fixed values for the diffusivity and the viscosity. In the horizontal, $\nu_h = 5$ m^2 s^{-1}. In the vertical, $\nu_z = 10^{-5}$ m^2 s^{-1}. To study the time evolution of the tracer concentration variance along the pycnocline, east–west-oriented streaks of tracer are initialized along different isopycnals, namely at $\sigma = 25.44$, 26.19, 26.54, and 26.76 across the zonal extent of the domain. The streaks, of 1-km width and initial tracer concentration 1 unit, are placed at $y = 80$ km from the southern boundary (i.e., below the surface ML front). To estimate effective diffusivity, a tracer with concentration varying linearly from 1 at the southern boundary to 0 at the northern boundary and spread along the entire domain is initialized along the $\sigma = 25.44$, 26.19, 26.54, and 26.76 isopycnals. For the reference integration, the four isopycnal surfaces have initial depths of 216.59, 256.88, 302.72, and 354.87 m, respectively. At the northern and southern boundary, the tracer is subject to the boundary condition $\partial C/\partial y = 0$.

REFERENCES

Abernathey, R., J. Marshall, M. Mazloff, and E. Shuckburgh, 2010: Enhancement of mesoscale eddy stirring at steering levels in the Southern Ocean. *J. Phys. Oceanogr.,* **40,** 170–184.

Batchelor, G. K., 1950: The application of the similarity theory of turbulence to atmospheric diffusion. *Quart. J. Roy. Meteor. Soc.,* **76,** 133–146.

Bennett, A. F., 1984: Relative dispersion: Local and nonlocal dynamics. *J. Atmos. Sci.,* **41,** 1881–1886.

Billant, P., and J.-M. Chomaz, 2000a: Experimental evidence for a new instability of a vertical columnar vortex pair in a strongly stratified fluid. *J. Fluid Mech.,* **418,** 167–188.

——, and ——, 2000b: Theoretical analysis of the zigzag instability of a vertical columnar vortex pair in a strongly stratified fluid. *J. Fluid Mech.,* **419,** 29–63.

Bishop, C. H., 1993: On the behavior of baroclinic waves undergoing horizontal deformation. I The 'RT' phase diagram. *Quart. J. Roy. Meteor. Soc.,* **119,** 221–240.

Boccaletti, G., R. Ferrari, and B. Fox-Kemper, 2007: Mixed layer instabilities and restratification. *J. Phys. Oceanogr.,* **37,** 2228–2250.

Capet, X., J. C. McWilliams, M. J. Molemaker, and A. F. Shchepetkin, 2008a: Mesoscale to submesoscale transition in the California Current system. Part I: Flow structure, eddy flux, and observational tests. *J. Phys. Oceanogr.,* **38,** 29–43.

——, ——, ——, and ——, 2008b: Mesoscale to submesoscale transition in the California Current system. Part II: Frontal processes. *J. Phys. Oceanogr.,* **38,** 44–64.

——, ——, ——, and ——, 2008c: Mesoscale to submesoscale transition in the California Current system. Part III: Energy balance and flux. *J. Phys. Oceanogr.,* **38,** 2256–2269.

Eady, E. T., 1949: Long waves and cyclone waves. *Tellus,* **1,** 33–52.

Einstein, A., 1905: Ueber die von der molekularkinetischen Theorie der Waerme geforderte Bewegung von in ruhenden Fluessigkeiten suspendierten Teilchen. *Ann. Phys.,* **322,** 549–560.

Eldevik, T., and K. B. Dysthe, 2002: Spiral eddies. *J. Phys. Oceanogr.,* **32,** 851–869.

Er-El, J., and R. L. Peskin, 1981: Relative diffusion of constant-level balloons in the Southern Hemisphere. *J. Atmos. Sci.,* **38,** 2264–2274.

Ferrari, R., and M. Nikurashin, 2010: Suppression of eddy mixing across jets in the Southern Ocean. *J. Phys. Oceanogr.,* **40,** 1501–1519.

Fjørtoft, R., 1950: Application of integral theorems in deriving criteria of stability for laminar flows and for the baroclinic circular vortex. *Geofys. Publ.,* **17,** 5–32.

Fox-Kemper, B., R. Ferrari, and R. Hallberg, 2008: Parameterization of mixed layer eddies. Part I: Theory and diagnosis. *J. Phys. Oceanogr.,* **38,** 1145–1165.

Garrett, C., 1983: On the initial streakiness of a dispersing tracer in two- and three-dimensional turbulence. *Dyn. Atmos. Oceans,* **7,** 265–277.

Haine, T. W. N., and J. Marshall, 1998: Gravitational, symmetric, and baroclinic instability of the ocean mixed layer. *J. Phys. Oceanogr.,* **28,** 634–658.

Haynes, P. H., 2001: Vertical shear plus horizontal stretching as a route to mixing. *Proc. 12th 'Aha Huliko'a Hawaiian Winter Workshop,* Manoa, HI, University of Hawaii, 70–73.

——, and J. Anglade, 1997: The vertical-scale cascade in atmospheric tracers due to large-scale differential advection. *J. Atmos. Sci.,* **54,** 1121–1136.

——, and E. Shuckburgh, 2000a: Effective diffusivity as a diagnostic of atmospheric transport 1. Stratosphere. *J. Geophys. Res.,* **105,** 22 777–22 794.

——, and ——, 2000b: Effective diffusivity as a diagnostic of atmospheric transport 2. Troposphere and lower stratosphere. *J. Geophys. Res.,* **105,** 22 795–22 810.

Held, I. M., R. T. Pierrehumbert, S. T. Garner, and K. L. Swanson, 1995: Surface quasi-geostrophic dynamics. *J. Fluid Mech.,* **282,** 1–20.

Herterich, K., and K. Hasselmann, 1982: The horizontal diffusion of tracers by surface waves. *J. Phys. Oceanogr.,* **12,** 704–711.

Holmes-Cerfon, M., O. Buehler, and R. Ferrari, 2011: Particle dispersion by random waves in the rotating Boussinesq system. *J. Fluid Mech.,* **670,** 150–175.

Hoskins, B. J., and F. P. Bretherton, 1972: Atmospheric frontogenesis models: Mathematical formulation and solution. *J. Atmos. Sci.,* **29,** 11–37.

Houghton, R. W., 1997: Lagrangian flow at the foot of a shelfbreak front using a dye tracer injected into the bottom boundary layer. *Geophys. Res. Lett.,* **24,** 2035–2038.

Kamykowski, D., and S.-J. Zentara, 1986: Predicting plant nutrient concentrations from temperature and sigma-*t* in the upper kilometer of the world ocean. *Deep-Sea Res.,* **33A,** 89–105.

Koszalka, I., J. H. LaCasce, and K. A. Orvik, 2009: Relative dispersion in the Nordic Seas. *J. Mar. Res.,* **67,** 411–433.

Kraichnan, R. H., 1967: Inertial ranges of two-dimensional turbulence. *Phys. Fluids,* **10,** 1417–1423.

——, and D. Montgomery, 1980: Two-dimensional turbulence. *Rep. Prog. Phys.,* **43,** 547–619.

Kunze, E., 2001: Waves: Vortical mode. *Encyclopedia of Ocean Sciences,* S. T. J. Steele and K. Turekian, Eds., Academic Press, 3174–3178.

LaCasce, J. H., 2008: Statistics from Lagrangian observations. *Prog. Oceanogr.,* **77,** 1–29.

——, and A. Bower, 2000: Relative dispersion in the subsurface North Atlantic. *J. Mar. Res.,* **58,** 863–894.

——, and A. Mahadevan, 2006: Estimating subsurface horizontal and vertical velocities from sea-surface temperature. *J. Mar. Res.,* **64,** 695–721.

Lacorata, G., E. Aurell, B. Legras, and A. Vulpiani, 2004: Evidence for a $k^{-5/3}$ spectrum from the EOLE Lagrangian balloons in the low stratosphere. *J. Atmos. Sci.,* **61,** 2936–2942.

Ledwell, J. R., A. J. Watson, and C. S. Law, 1998: Mixing of a tracer in the pycnocline. *J. Geophys. Res.,* **103,** 21 499–21 529.

——, T. F. Duda, M. A. Sundermeyer, and H. E. Seim, 2004: Mixing in a coastal environment: 1. A view from dye dispersion. *J. Geophys. Res.,* **109,** C10013, doi:10.1029/2003JC002194.

Levitus, S., 1982: *Climatological Atlas of the World Ocean*. NOAA Prof. Paper 13, 173 pp and 17 microfiche.

Levy, M., P. Klein, and A.-M. Treguier, 2001: Impacts of submesoscale physics on phytoplankton production and subduction. *J. Mar. Res.,* **59,** 535–565.

Lewis, M. R., W. G. Harrison, N. S. Oakey, D. Hebert, and T. Platt, 1986: Vertical nitrate fluxes in the oligotrophic ocean. *Science,* **234,** 870–873.

Lin, J.-T., 1972: Relative dispersion in the enstrophy-cascading inertial range of homogeneous two-dimensional turbulence. *J. Atmos. Sci.,* **29,** 394–395.

Lumpkin, R., and S. Elipot, 2010: Surface drifter pair spreading in the North Atlantic. *J. Geophys. Res.,* **115,** C12017, doi:10.1029/2010JC006338.

Mahadevan, A., 2006: Modeling vertical motion at ocean fronts: Are nonhydrostatic effects relevant at submesoscales? *Ocean Modell.,* **14,** 222–240.

——, and A. Tandon, 2006: An analysis of mechanisms for submesoscale vertical motion at ocean fronts. *Ocean Modell.,* **14,** 241–256.

——, J. Oliger, and R. L. Street, 1996a: A nonhydrostatic mesoscale ocean model. Part I: Well-posedness and scaling. *J. Phys. Oceanogr.,* **26,** 1868–1880.

——, ——, and ——, 1996b: A nonhydrostatic mesoscale ocean model. Part II: Numerical implementation. *J. Phys. Oceanogr.,* **26,** 1881–1900.

——, A. Tandon, and R. Ferrari, 2010: Rapid changes in mixed layer stratification driven by submesoscale instabilities and winds. *J. Geophys. Res.,* **115,** C03017, doi:10.1029/2008JC005203.

Marshall, J., E. Shuckburgh, H. Jones, and C. Hill, 2006: Estimates and implications of surface eddy diffusivity in the Southern Ocean derived from tracer transport. *J. Phys. Oceanogr.,* **36,** 1806–1821.

McWilliams, J. C., F. Colas, and M. J. Molemaker, 2009a: Cold filamentary intensification and oceanic surface convergence lines. *Geophys. Res. Lett.,* **36,** L18602, doi:10.1029/2009GL039402.

——, M. J. Molemaker, and E. I. Olafsdottir, 2009b: Linear fluctuation growth during frontogenesis. *J. Phys. Oceanogr.,* **39,** 3111–3129.

Molemaker, M. K., J. C. McWilliams, and I. Yavneh, 2005: Baroclinic instability and loss of balance. *J. Phys. Oceanogr.,* **35,** 1505–1517.

Morel, P., and M. Larcheveque, 1974: Relative dispersion of constant-level balloons in the 200-mb general circulation. *J. Atmos. Sci.,* **31,** 2189–2196.

Munk, W., 1981: Internal waves and small-scale processes. *Evolution of Physical Oceanography,* B. Warren and C. Wunsch, Eds., MIT Press, 264–291.

Nagai, T., A. Tandon, and D. L. Rudnick, 2006: Two-dimensional ageostrophic secondary circulation at ocean fronts due to vertical mixing and large-scale deformation. *J. Geophys. Res.,* **111,** C09038, doi:10.1029/2005JC002964.

Nakamura, N., 1996: Two-dimensional mixing, edge formation, and permeability diagnosed in an area coordinate. *J. Atmos. Sci.,* **53,** 1524–1537.

——, and J. Ma, 1997: Modified Lagrangian-mean diagnostics of the stratospheric polar vortices 2. Nitrous oxide and seasonal barrier migration in the cryogenic limb array etalon spectrometer and SKYHI general circulation model. *J. Geophys. Res.,* **102,** 25 721–25 735.

Okubo, A., 1970: Horizontal dispersion of floatable particles in the vicinity of velocity singularity such as convergences. *Deep-Sea Res.,* **17,** 445–454.

——, 1971: Oceanic diffusion diagrams. *Deep-Sea Res.,* **18,** 789–802.

Ollitrault, M., C. Gabillet, and A. C. de Verdiere, 2005: Open ocean regimes of relative dispersion. *J. Fluid Mech.,* **533,** 381–407.

Pedlosky, J., 1987: *Geophysical Fluid Dynamics*. 2nd ed. Springer, 728 pp.

Planas, D., S. Agusti, C. M. Duarte, T. C. Granata, and M. Merino, 1999: Nitrate uptake and diffusive nitrate supply in the Central Atlantic. *Limnol. Oceanogr.,* **44,** 116–126.

Polzin, K. L., and R. Ferrari, 2004: Lateral dispersion in NATRE. *J. Phys. Oceanogr.,* **34,** 247–257.

Richardson, L. F., 1926: Atmospheric diffusion shown on a distance-neighbour graph. *Proc. Roy. Soc. London,* **110,** 709–737.

Rudnick, D. L., and R. Ferrari, 1999: Compensation of horizontal temperature and salinity gradients in the ocean mixed layer. *Science,* **283,** 526–529.

Shuckburgh, E., and P. Haynes, 2003: Diagnosing transport and mixing using a tracer-based coordinate system. *Phys. Fluids,* **15,** 3342–3357.

——, H. Jones, J. Marshall, and C. Hill, 2009: Robustness of an effective diffusivity diagnostic in oceanic flows. *J. Phys. Oceanogr.,* **39,** 1993–2009.

Smith, K. S., and G. K. Vallis, 2001: The scales and equilibration of midocean eddies: Freely evolving flow. *J. Phys. Oceanogr.,* **31,** 554–571.

——, and R. Ferrari, 2009: The production and dissipation of compensated thermohaline variance by mesoscale stirring. *J. Phys. Oceanogr.,* **39,** 2477–2501.

——, and J. Marshall, 2009: Evidence for enhanced eddy mixing at middepth in the Southern Ocean. *J. Phys. Oceanogr.,* **39,** 50–69.

Spall, M., 1997: Baroclinic jets in confluent flows. *J. Phys. Oceanogr.,* **27,** 381–402.

Stommel, H., 1949: Horizontal diffusion due to oceanic turbulence. *J. Mar. Res.,* **8,** 199–225.

Stone, P., 1966: On non-geostrophic baroclinic stability. *J. Atmos. Sci.,* **23,** 390–400.

——, 1970: On non-geostrophic baroclinic stability: Part II. *J. Atmos. Sci.,* **27,** 721–726.

——, 1971: Baroclinic stability under non-hydrostatic conditions. *J. Fluid Mech.,* **46,** 659–671.

Sundermeyer, M. A., and J. F. Price, 1998: Lateral mixing and the North Atlantic Tracer Release Experiment: Observations and numerical simulations of Lagrangian particles and passive tracer. *J. Geophys. Res.,* **103,** 21 481–21 497.

——, and J. R. Ledwell, 2001: Lateral dispersion over the continental shelf: Analysis of dye-release experiments. *J. Geophys. Res.,* **106,** 9603–9622.

——, and M.-P. Lelong, 2005: Numerical simulations of lateral dispersion by the relaxation of diapycnal mixing events. *J. Phys. Oceanogr.,* **35,** 2368–2386.

——, J. R. Ledwell, N. S. Oakey, and B. J. W. Greenan, 2005: Stirring by small-scale vortices caused by patchy mixing. *J. Phys. Oceanogr.,* **35,** 1245–1262.

Tandon, A., and C. Garrett, 1994: Mixed layer restratification due to a horizontal density gradient. *J. Phys. Oceanogr.,* **24,** 1419–1424.

——, and ——, 1995: Geostrophic adjustment and restratification of a mixed layer with horizontal gradients above a stratified layer. *J. Phys. Oceanogr.,* **25,** 2229–2241.

Taylor, G. I., 1921: Diffusion by continuous movements. *Proc. Roy. Soc. London,* **20,** 196–211.

——, 1953: Dispersion of soluble matter in solvent flowing slowly through a tube. *Proc. Roy. Soc. London,* **219,** 186–203.

Thiffeault, J.-L., 2008: Scalar decay in chaotic mixing. *Transport and Mixing in Geophysical Flows,* J. B. Weiss and A. Provenzale, Eds., Lecture Notes in Physics, Vol. 744, Springer, 3–35.

Thomas, L., and C. M. Lee, 2005: Intensification of ocean fronts by down-front winds. *J. Phys. Oceanogr.,* **35,** 1086–1102.

Weiss, J., 1991: The dynamics of enstrophy transfer in two-dimensional hydrodynamics. *Physica D,* **48,** 273–294.

Winters, K. B., and E. A. D'Asaro, 1996: Diascalar flux and the rate of fluid mixing. *J. Fluid Mech.,* **317,** 179–193.

Young, W. R., 1994: The subinertial mixed layer approximation. *J. Phys. Oceanogr.,* **24,** 1812–1826.

——, P. B. Rhines, and C. J. Garrett, 1982: Shear-flow dispersion, internal waves and horizontal mixing in the ocean. *J. Phys. Oceanogr.,* **12,** 515–527.